Regional coupled ocean–atmosphere downscaling in the Southeast Pacific: impacts on upwelling, mesoscale air–sea fluxes, and ocean eddies

Dian A. Putrasahan · Arthur J. Miller · Hyodae Seo

Abstract Ocean–atmosphere coupling in the Humboldt Current System (HCS) of the Southeast Pacific is studied using the Scripps Coupled Ocean–atmosphere Regional (SCOAR) model, which is used to downscale the National Center for Environmental Prediction (NCEP) Reanalysis-2 (RA2) product for the period 2000–2007 at 20-km resolution. An interactive 2-D spatial smoother within the sea-surface temperature (SST)–flux coupler is invoked in a separate run to isolate the impact of the mesoscale (~50–200 km, in the oceanic sense) SST field felt by the atmosphere in the fully coupled run. For the HCS, SCOAR produces seasonal wind stress and wind stress curl patterns that agree better with QuikSCAT winds than those from RA2. The SCOAR downscaled wind stress distribution has substantially different impacts on the magnitude and structure of wind-driven upwelling processes along the coast compared to RA2. Along coastal locations such as Arica and Taltal, SCOAR and RA2 produce seasonally opposite signs in the total wind-driven upwelling transport. At San Juan, SCOAR shows that upwelling is mainly due to coastal

Ekman upwelling transport, while in RA2 upwelling is mostly attributed to Ekman pumping. Fully coupled SCOAR shows significant SST–wind stress coupling during fall and winter, while smoothed SCOAR shows insignificant coupling throughout, indicating the important role of ocean mesoscale eddies on air–sea coupling in HCS. Coupling between SST, wind speed, and latent heat flux is incoherent in large-scale coupling and full coupling mode. In contrast, coupling between these three variables is clearly identified for oceanic mesoscales, which suggests that mesoscale SST affects latent heat directly through the bulk formulation, as well as indirectly through stability changes on the overlying atmosphere, which affects surface wind speeds. The SST–wind stress and SST–heat-flux couplings, however, fail to produce a strong change in the ocean eddy statistics. No rectified effects of ocean–atmosphere coupling were identified for either the atmospheric or oceanic mean conditions, suggesting that mesoscale coupling is too weak in this region to strongly alter the basic climate state.

Keywords Eastern boundary current · Humboldt Current · Peru current · VOCALS · Coupled ocean–atmosphere feedbacks · Mesoscale eddies · Surface fluxes

D. A. Putrasahan (✉) · A. J. Miller
Scripps Institution of Oceanography, University of California,
San Diego, La Jolla, CA 92093-0224, USA
e-mail: dputrasahan@rsmas.miami.edu

H. Seo
Woods Hole Oceanographic Institution,
Woods Hole, MA 02543, USA

Present Address:
D. A. Putrasahan
Rosenstiel School of Marine and Atmospheric Sciences,
University of Miami, Miami, FL 33149-1098, USA

1 Introduction

The climate of the Southeast Pacific involves important feedbacks between atmospheric circulation, sea-surface temperature (SST), clouds, ocean heat transport, aerosols, and coastal orography, bathymetry, and geometry (Wood et al. 2011). This region is vitally important to global climate because of its effect on the Walker Cell, which controls both the mean state of the tropical Pacific and El Nino–Southern

Oscillation variability in key ways (e.g., Ma et al. 1996). It also includes the Humboldt Current System (HCS), an eastern boundary current (EBC) system that supports a productive ecosystem that provides roughly 20 % of the world's fish catch (Sherman and Hempel 2008; Overland et al. 2010).

While global and regional climate models work well in simulating ocean circulation and atmospheric flow patterns on the large scale, significant biases still occur, especially in EBC regions, such as off the west coast of South America (Large and Danabasoglu 2006). A major experimental and modeling program called VAMOS Ocean Cloud Atmosphere Land Studies (VOCALS) was initiated to investigate the dynamics of various feedbacks in controlling the climate in this hotspot region, and numerous results have been obtained toward those goals (Wood et al. 2011).

Here we present a regional coupled modeling study that was motivated by the VOCALS program along with other recent studies that have uncovered interesting impacts of mesoscale SST anomalies on the atmospheric boundary layer (Chelton et al. 2001; Xie 2004; Seo et al. 2007a; Small et al. 2008; Minobe et al. 2010; Chelton and Xie 2010). Our numerical experiments are designed to allow for mesoscale (~50–200 km in the oceanic sense) SST feedbacks on the atmosphere in the Southeast Pacific region so that we can evaluate their impact on modifying local oceanic and atmospheric processes in the HCS of the Southeast Pacific.

Quantification of air–sea coupling using SST gradients and wind stress derivatives has been widely accomplished with many satellite observations over the world's ocean, including the Gulf Stream, California Current System (CCS), Agulhas Return Current, tropical Atlantic Ocean, and the Antarctic Circumpolar Current (Chelton et al. 2004, 2007; O'Neill et al. 2003, 2005; Samelson et al. 2006). However, such an analysis has not been performed over the Southeast Pacific region, off the coasts of Peru and Chile, because it was thought to exhibit only weak coupling. But even weak local feedbacks between mesoscale ocean variability and the atmosphere in this region could potentially rectify to produce a response that has important remote influences on global climate through changes in the Walker Cell.

Historical results indicate that the atmosphere predominantly drives large-scale variability of SST via latent heat and sensible heat flux (Cayan 1992), which suggests that the ocean is mainly subservient to the atmosphere. This is supported by the generally negative correlation of SST and winds found during winter months (Wallace et al. 1990). However, the presence of oceanic fronts proves to counter to those results, at least on the oceanic mesoscale (Nakamura et al. 2004; Nonaka and Xie 2003). For example, observations have shown that areas with colder SST or cold filaments are generally coincident with wind stress minima and places with warmer SST covary with strong wind stress (Wallace et al. 1989; Chelton et al. 2001; Xie 2004; Vecchi et al. 2004; Small et al. 2008). This leads to a positive relation between wind stress divergence (curl) and downwind (crosswind) SST gradient when winds blow perpendicular (parallel) to an SST front (e.g., Chelton et al. 2004). Observations also have indicated coupling between SST and surface heat fluxes (e.g., Vecchi et al. 2004), and models have shown that latent heat fluxes out of the ocean have a positive correlation with mesoscale SSTs in various parts of the World Ocean (Thum et al. 2002; Liu et al. 2007; Seo et al. 2007a, 2008; Haack et al. 2008; Bryan et al. 2010).

In this study, we use regional coupled ocean–atmosphere models to downscale a global atmospheric analysis product in the Southeast Pacific from the time period from 2000 to 2007. We first validate the fully coupled model by comparing the wind stress fields with those of satellite observations. We then evaluate the impact of the model-predicted wind stress fields on coastal Ekman upwelling and open-ocean Ekman pumping because the results are important for nutrient input for sustaining the ecosystem.

Next, we focus on the magnitude and consequences of mesoscale ocean–atmosphere boundary layer coupling, in which SST affects the stability of the atmospheric boundary and concomitantly alters the surface stresses and surface heat fluxes. This part of the analysis is facilitated by invoking a recently developed technique (Putrasahan 2012; Putrasahan et al. 2013) with an analogous coupled run that removes the impact of the oceanic mesoscale SST on coupling. Finally, in turn, we assess the impacts of the SST-driven flux anomalies on ocean eddy statistics. The coupled runs are also compared, as needed for clarification, with uncoupled versions of the atmosphere and ocean.

Section 2 discusses the regional coupled and uncoupled models used to study ocean–atmosphere interactions in this EBC. Section 3 contains several studies pertaining to the HCS. Presented first is a study on the impact of downscaling on the model wind products, followed by a study of the consequent wind-driven upwelling along the coast of Peru and Chile. Next is an assessment of SST–wind stress coupling in Peruvian waters. The third study focuses on understanding the impact of mesoscale SST on wind speed and latent heat flux. The fourth examines the effects of full coupling versus large-scale coupling on ocean eddy statistics. Section 4 gives a summary and discussion.

2 The SCOAR model runs

The Scripps Coupled Ocean–atmosphere Regional (SCOAR) model is employed to perform coupled ocean–atmosphere interaction studies in the HCS. This model was

developed by Seo et al. (2007a). The model consists of the Experimental Climate Prediction Center (ECPC) Regional Spectral Model (RSM) as the atmospheric component, the Regional Ocean Modeling System (ROMS) as the oceanic part, and a flux–SST coupler to bridge the two. This model is chosen because it has shown to be effective in capturing mesoscale features in tropical and mid-latitudinal oceans (Seo et al. 2006, 2007a, b, 2008; Putrasahan et al. 2013).

ROMS is an incompressible, free-surface, hydrostatic, primitive equation ocean model that utilizes a horizontal, orthogonal, curvilinear grid and a generalized sigma-coordinate system that includes enhanced vertical resolution in the surface and bottom layers of the ocean (Shchepetkin and McWilliams 2005; Haidvogel et al. 2008). The K-profile parameterization vertical mixing scheme is used, along with a third-order upstream horizontal advection and a fourth-order centered vertical advection scheme for both tracers and momentum. Radiation nudging to open boundary conditions is used so that long-term integrations are more stable and nudging is adaptive to inflow/outflow ratio, meaning nudging is stronger on inflow than on outflow if the ratio is greater than 1. The 1950–2007 OFES (Ocean Global Climate Model for the Earth Simulator) hindcast monthly mean products (Sasaki et al. 2006) are used to force the lateral boundary conditions on ROMS.

ECPC-RSM, hereinafter denoted as RSM, is a hydrostatic, primitive equation atmospheric model that uses a terrain-following sigma-coordinate system. RSM was first developed by Juang and Kanamitsu (1994) at the National Center for Environmental Prediction (NCEP) and later revised and improved upon its dynamics and efficiency by Juang et al. (1997). Essentially, RSM provides regional details downscaled from the Global Spectral Model (GSM) that is physically and dynamically consistent with the NCEP/Department of Energy Reanalysis (RA2) model (Kanamitsu et al. 2002a). This is done by nesting RSM non-interactively and one-way within GSM such that GSM forces RSM along the lateral boundaries. The boundary layer (BL) parameterization in RSM uses a nonlocal diffusion scheme (Hong and Pan 1996) that couples strongly with the surface layer physics. Above the BL, in the free troposphere, a local diffusion scheme is used. For this study, the Relaxed Arakawa–Schubert scheme is used for deep convective parameterization along with Haack shallow convection scheme. The Yonsei University cloud water prediction scheme (Lim and Hong 2010) is used, which follows a double-moment cloud microphysics scheme that takes water vapor, cloud water, and rain water as prognostic variables. The default setting of spectral tendency damping scheme was turned off to allow features of fields greater than 2,000 km within the domain to freely evolve in the presence of ocean–atmosphere coupling. Kanamitsu et al. (2002b) provides more details regarding the model physics.

The flux–SST coupler (Seo et al. 2007a) works in a sequential manner, such that RSM and ROMS run individually and alternately, exchanging forcing fields daily. Surface flux fields driving the ocean invoke the Tropical Ocean Global Atmosphere Coupled Ocean Atmosphere Response Experiment bulk parameterization (Fairall et al. 1996) to calculate the surface momentum, latent, and sensible heat fluxes from near-surface meteorological variables with ROMS SST. RSM is only forced on the surface by SST, which is given by ROMS. This exchange of SST and surface fluxes between the ocean and atmosphere within SCOAR allows the study of mesoscale coupled air–sea feedbacks.

The model domain covers a regional grid from 88 W to 68 W and 8 S to 38 S. The atmospheric and ocean model have the same horizontal grid with 20 km resolution. However, the atmosphere has 28 vertical layers whilst the ocean has 30 layers. The vertical coordinates for the ocean model were stretched to give higher resolution to the surface layers. The ocean spin up (in uncoupled mode) is forced by RA2 winds from 1980 to 2000 to allow equilibration before any coupled runs are performed. The coupled run is a downscaling of the RA2 from 2000 to 2007. Daily averages are saved for both the oceanic and atmospheric state. Note that since the ocean eddies are randomly generated in the model and have no correlation to the ocean eddies observed in nature, a direct deterministic comparison of the downscaled mesoscale ocean–atmosphere variations with observations is not possible. Instead, the statistical properties of the model and natural systems must be compared.

Putrasahan et al. (2013) recently introduced a new method to investigate mesoscale SST influence in a coupled framework. This strategy is also employed here. The technique invokes an interactive SST smoother in a "smoothed SCOAR" run, which is applied solely to the SST that is felt by the atmosphere over the same time period and with the same resolution as the fully coupled "control SCOAR" run. Note that the actual SST in the ocean model is left unchanged but evolves instead under the influence of an atmosphere that has seen only the smoothed SST field. In the experiments that remove the mesoscale air–sea interactions, an online 2-D spatial, locally weighted scatterplot smoothing (lowess) filter (Schlax et al. 2001) is applied to the SST field that forces RSM at each coupling step. This procedure effectively allows large-scale SST coupling to be preserved while extinguishing the mesoscale eddy impacts on the atmospheric boundary layer. This technique allows us to separate the spatial scales of air–sea coupling by comparing with the fully coupled run. Here we use a 2.5° lowess filter, which yields a cutoff wavelength of 1.5° (~150 km) in latitude and longitude. As such, features up to 150 km are considered "mesoscale" and greater than 150 km are referred to as "large scale." This allows for comparative

studies that provide a sense of how large-scale coupling differs from full coupling and extracts the importance of mesoscale coupling. The interactive smoothing technique can also be used to determine the impact of the SST-induced mesoscale flux anomalies on the ocean eddies themselves.

Figure 1 gives an example of the performance of the filter on the SST field for this HCS study. The top left and right panels show the averaged April 2007 SST field for control and smoothed SCOAR, respectively. The bottom left panel presents the difference between the two, which indicates that the filter effectively removes patterns and filaments of scales roughly 150 km and less. The bottom right panel shows the SST power spectrum of latitudinal band, 20 S–36 S, for control SCOAR and smoothed RSM. The power spectrum indicates that the filter preserves much of the energy at low wavenumber and rolls off as the wavenumber increases. The ratio of the power spectra of smoothed RSM and control SCOAR gives an estimate of the variance retained after smoothing, which provides a gauge of the cutoff wavelength for the filter. In this case, the filter cuts off ~80 % of the energy at wavelength of ~180 km.

We also used a deterministic approach to further isolate the effects of these mesoscale SST patterns on the atmosphere by applying the 2-D smoother upon the raw SST fields taken from the control SCOAR run. These daily smoothed SST fields are prescribed as surface forcing for the uncoupled atmosphere, "smoothed RSM," for an 8-year (2000–2007) daily response of the atmospheric state. The difference in the two runs highlights the influence of mesoscale SST on the overlying atmosphere, as well as isolating the mesoscale coupling effects. This direct-differencing comparison cannot be achieved by differencing control and smoothed SCOAR runs because the oceanic eddies are randomly generated in each case.

In addition, for study of the impact of coupling on ocean dynamics, an uncoupled run of ROMS is executed that is daily forced by spatially smoothed surface atmospheric fields from control SCOAR for the 2000–2007 time period. This run, designated as "smoothed ROMS" is used to assess the influence of spatially smoothed surface forcing on the ocean.

3 Mesoscale ocean–atmosphere coupling results
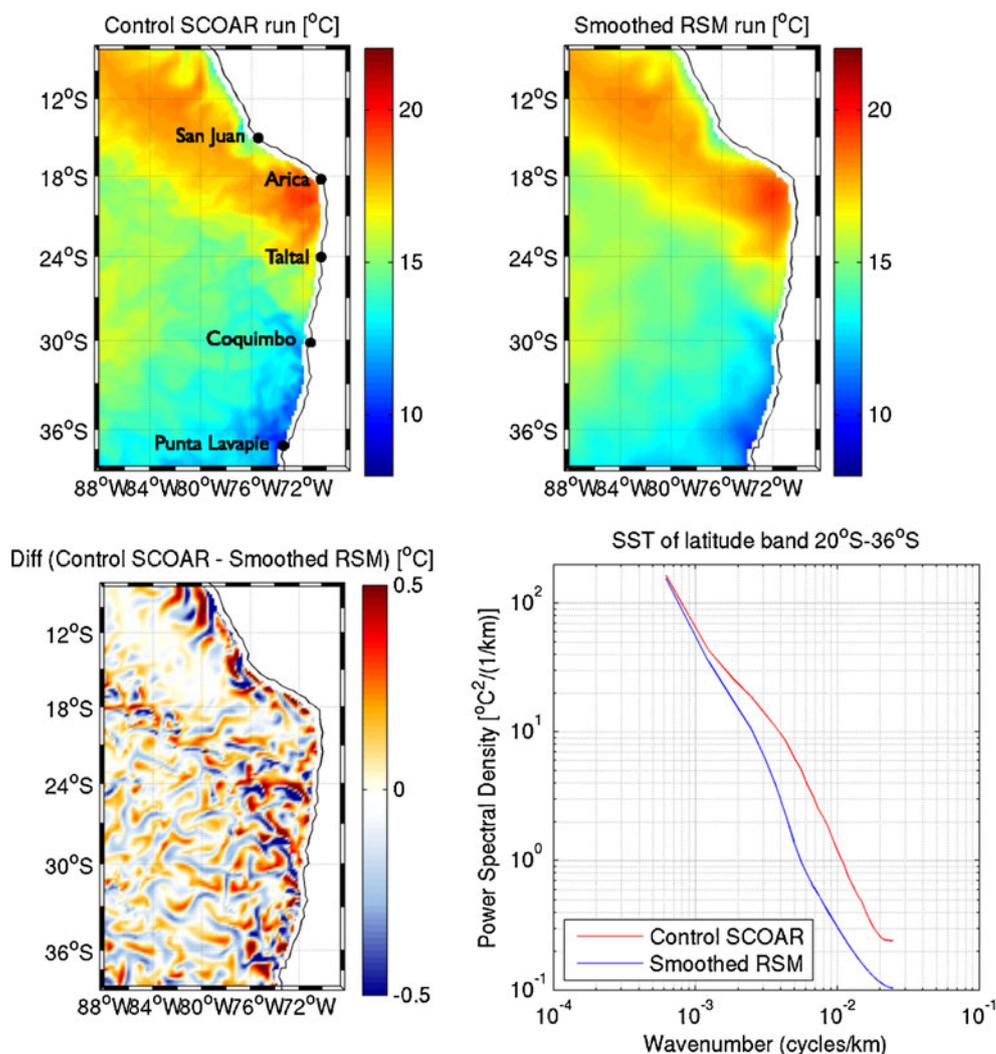
3.1 Downscaled wind stresses

We first address the capabilities of the SCOAR model to downscale the RA2 winds in this important region. The wind fields are validated with Quick Scatterometer (QuikSCAT) winds at 0.5° resolution (Liu 2002). Figure 2 shows the seasonal cycle of wind stress field averaged over

2000–2007, for satellite observations. Satellite-derived wind stress fields indicate a consistent southerly/southeasterly winds off the coast of Peru and Chile throughout the year, with variations of the strength and location of the maxima. There is an anticyclonic high around 85 W that migrates meridionally (about 30 S in summer and around 35 S in winter) and brings south–southwesterly winds to Chile at Punta Lavapie during winter and westerly winds in other seasons. Coastal atmospheric jets seasonally form around San Juan (Peru) during fall (April–May–June, AMJ) through winter (July–August–September, JAS). In Chile, the coastal atmospheric jets typically form during spring (October–November–December, OND) and summer (January–February–March, JFM) along Coquimbo and Punta Lavapie (Garreaud and Munoz 2005; Renault et al. 2009). Model-derived wind stress fields from SCOAR (Fig. 3) show similar spatial distribution and magnitude, which indicates the ability of SCOAR to downscale large-scale winds and provide the appropriate forcing over the ocean. For RA2 (Fig. 4), however, the location of the maximum wind stress field is shifted offshore, which would consequently affect the contribution of Ekman upwelling transport to the total upwelling, particularly along the coast.

The seasonal cycle of wind stress curl field derived from satellite observations is presented in Fig. 5. It shows that near and along the coast, wind stress curl fields are negative and extend to approximately 100 km offshore. Wind stress curl fields are generally positive further offshore from Chile and mostly negative further offshore from Peru. Negative wind stress curl in the Southern Hemisphere is associated with upwelling due to Ekman pumping. SCOAR (Fig. 6) exhibits similar spatial patterns of wind stress curl, with stronger and narrower negative wind stress curl hugging along the coast (likely due to the higher resolution of RSM compared to the observations). The exception is around San Juan and Coquimbo, where there is a positive wind stress curl along the coast. This indicates that the wind stress maximum is located right on the coast rather than just near the coast. For RA2 (Fig. 7), wind stress curl following the coastline is mostly negative and extends to about 600 km offshore, beyond which wind stress curl becomes positive throughout. During austral spring and summer, wind stress curl is positive along the coast in the southern part of the domain. The wider and more intense negative wind stress curl along the coast would impact the contribution of Ekman pumping on the total upwelling.

Taken together, these results show very good agreement of the spatial distribution and magnitude of the wind fields seen in SCOAR and observations. The corrective changes seen between the RA2 and downscaled winds demonstrates the ability of SCOAR to properly represent the regional winds by boundary-forced model dynamics.

Control SCOAR run [°C]

Smoothed RSM run [°C]

Diff (Control SCOAR - Smoothed RSM) [°C]

SST of latitude band 20°S-36°S
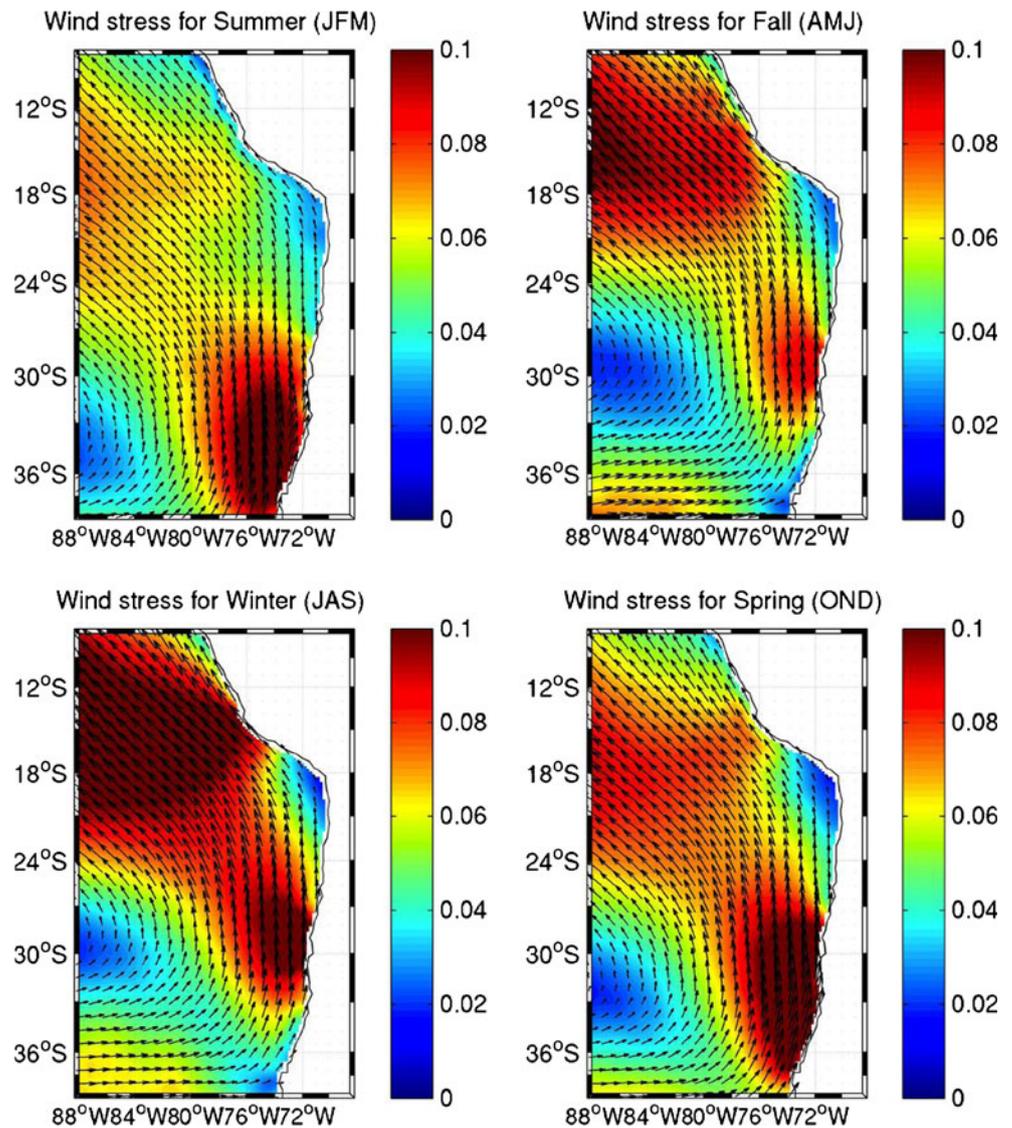
3.2 Wind-forced upwelling

We next compare the wind fields from SCOAR and the RA2 to investigate the contribution of coastal Ekman upwelling transport versus Ekman pumping transport (Smith 1968; Castelao and Barth 2006; Halpern 2002), to the total wind-driven upwelling in three key locations along the HCS coast. Satellite-observed winds over the ocean within 50 km of the coast are not as accurate, so wind-driven coastal upwelling based on satellite observations are not computed here.

Integration of the Ekman pumping velocity, w_{Ek}, over some distance offshore from each coastal grid point was performed to get units of transport (W_{Ek}, in cubic meter per second per meter of coast) that can be compared to coastal Ekman upwelling transport (M_{Ek}, in cubic meter per second per meter of coast). Over California Current System, the zero wind stress curl line extends to about 200–300 km offshore (Pickett and Paduan 2003), which indicates the extent of transport by Ekman pumping. Similarly, using satellite-derived wind stress curl fields over the Humboldt Current System, this would

extend to approximately 100–200 km offshore. An estimate of the total wind-driven upwelling is obtained by taking the sum of both transports ($T_{Ek}=M_{Ek}+W_{Ek}$).

We consider three locations (marked in Fig. 1) along the coast of Peru and Chile, namely San Juan, Arica, and Taltal, which have strong, weak, and moderate coastal upwelling and Ekman pumping fields, respectively, to exemplify key aspects of the impact of downscaling on the wind-forced upwelling fields. The coastal Ekman upwelling transport (CEUT=M_{Ek}), Ekman pumping transport (EPT=W_{Ek}), and total wind-driven upwelling transport are computed based on the wind forcing from SCOAR and the RA2. For the CEUT along each location, the alongshore wind stress component of the grid point right next to the coast is used. Positive (negative) Ekman upwelling transport indicates offshore (onshore) transport that induces an equivalent upwelling (downwelling) right at the coast. For the transport due to Ekman pumping, the Ekman pumping velocity is integrated from the coast to approximately 100 km offshore. Again, positive (negative)
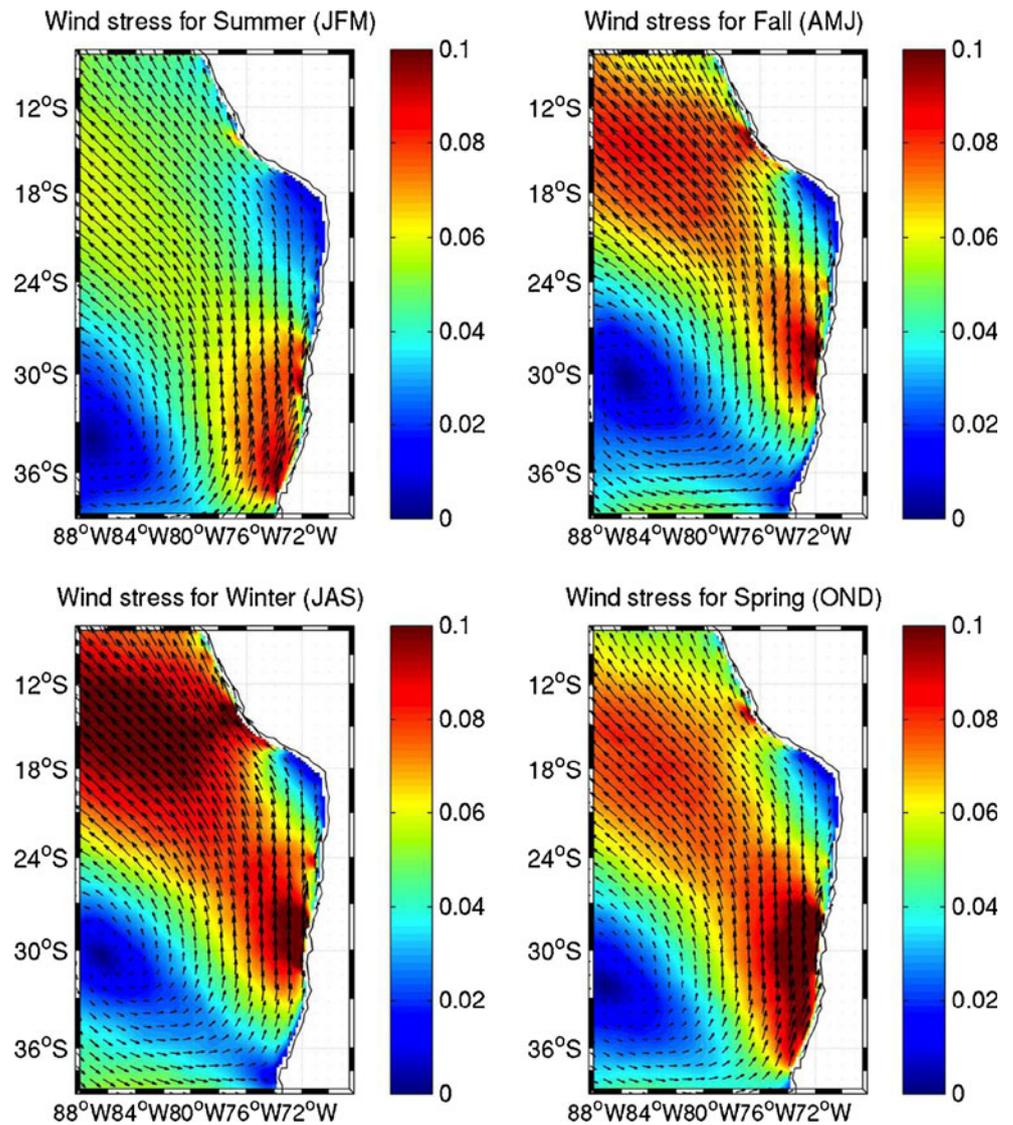
transport is associated with upwelling (downwelling) waters.

At San Juan, Fig. 8 shows the CEUT, EPT, and total wind-driven upwelling based on SCOAR and RA2. Here, SCOAR exhibits a consistent, positive CEUT with a distinct seasonal cycle that peaks during the wintertime. The high wind stress upon the waters at this location produces CEUT of roughly 1.5 $m^3/s/m$ in summer and about 4 $m^3/s/m$ in winter. RA2, on the other hand, does not have a seasonal cycle in CEUT, but it has a rather constant, equatorward, alongshore wind that produces about 0.5 $m^3/s/m$ CEUT. With respect to EPT, the location of the wind stress maximum is particularly important. SCOAR reveals a maximum on the coast and weakening of winds within about 100 km offshore, which leads to negative EPT. The EPT also has a seasonal cycle that ranges between −1.4 (in winter) to −0.2 $m^3/s/m$ (in summer). RA2 has a similar seasonal and range in magnitude of EPT, but of the opposite sign. This

indicates strengthening winds while extending offshore. A seasonal cycle is evident in the total transport for both SCOAR and RA2. During winter, total transport in SCOAR is greater than RA2 by a factor of 1.5 to 2 and only slightly greater by about 10 % during summer. This will have implications on the nutrient flux brought to the surface ocean and affect the nutrient availability for biological production. CEUT contributes about 80 % of the total transport in SCOAR, while EPT contributes about 60 % of the total transport in RA2. This shows that while both SCOAR and RA2 can induce a similar seasonal cycle in total upwelling transport, the mechanism for the upwelling is different in the two wind forcing products.

Arica is situated at the border of Peru and Chile, on a geographical bend that is characterized by a wind stress minimum. Figure 9 reflects a steady, equatorward alongshore wind that gives rise to a constant 0.2 $m^3/s/m$ CEUT in SCOAR. RA2 shows a seasonal reversal of winds at the

Fig. 3 Seasonal wind stress field (in Newton per square meter) over the HCS region averaged from 2000 to 2007 for SCOAR. Austral summer (JFM; *top left*), fall (AMJ; *top right*), winter (JAS; *bottom left*), and spring (OND; *bottom right*)
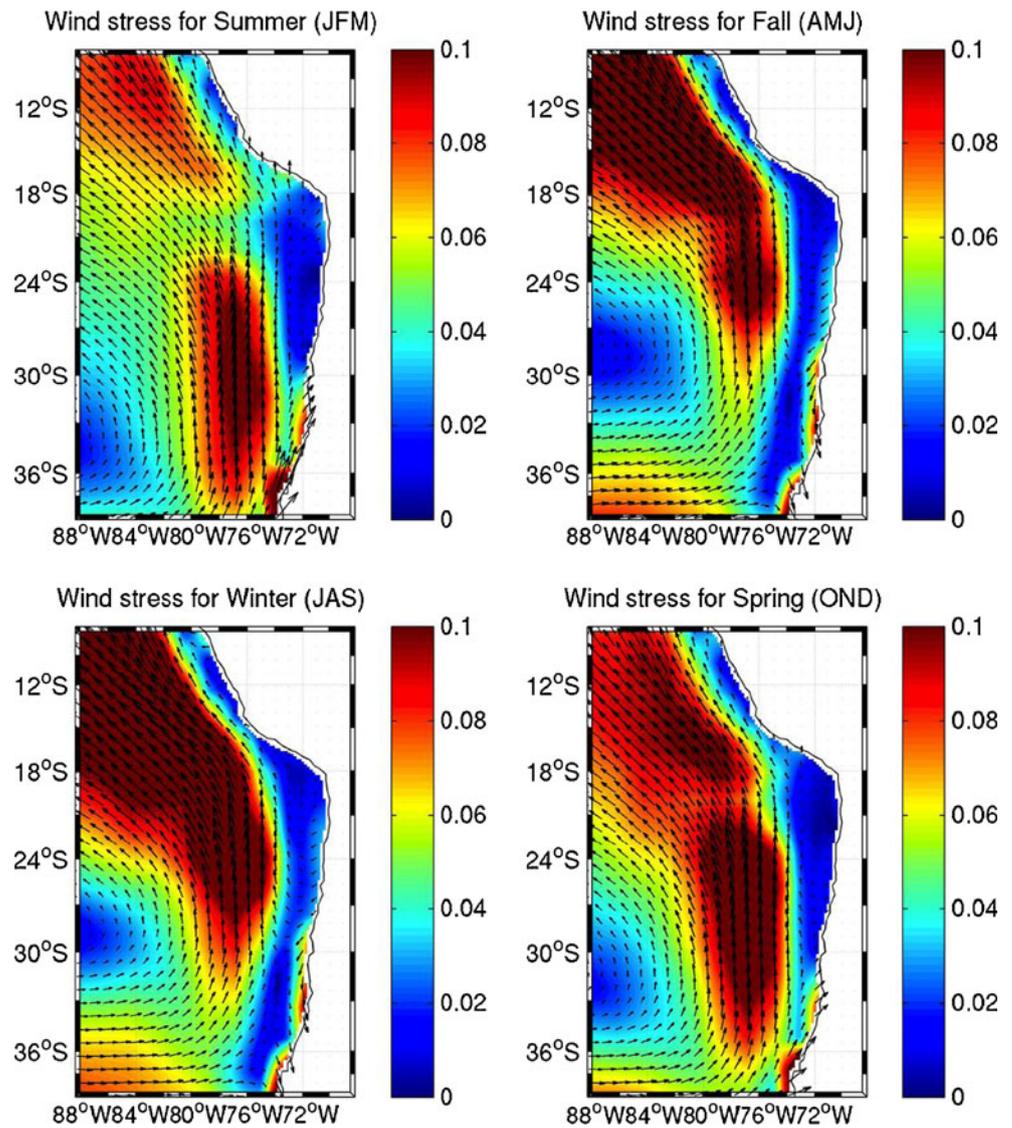
coast that induces offshore transport during summer and onshore transport during winter, with CEUT of roughly ±0.5 m³/s/m. RA2 also shows a seasonal cycle in EPT that in contrast to CEUT and produces negative EPT in summer and positive EPT in winter, with EPT magnitude of about ±0.3 m³/s/m. SCOAR has a marginally variable EPT centered around 0.1 m³/s/m. As such, the total transport for SCOAR is about 0.3 m³/s/m throughout the whole time series. For RA2, the CEUT provides about 70 % of the total transport, thereby allowing upwelling (downwelling) favorable conditions during summer (winter). This reflects the importance of the spatial distribution of wind forcing used as it can produce quite different conditions for nutrient flux.

South of Arica, the coastline is oriented north–south over roughly 800 km, and Taltal provides a typical example for this stretch. For the coastal water off Taltal, a time series of the total wind-driven upwelling transport and its two components are shown in Fig. 10. In SCOAR, weak winds

uniformly blow northward and produce CEUT of about 0.3 ±0.1 m³/s/m. In RA2, the seasonal cycle of the winds bring stronger negative CEUT of about −0.6 m³/s/m during fall season. In contrast, EPT in this area has a seasonal cycle in SCOAR that ranges between 0.3 and 1.2 m³/s/m with its peak in winter, while in RA2, it is a more steady 0.3± 0.1 m³/s/m EPT. As a result, the combined transport in SCOAR produces upwelling favorable conditions throughout, with a seasonal cycle that ranges between 0.5 and 1.5 m³/s/m. On the other hand, the total transport in RA2 flips between negative and positive. From 2000 to mid-2003, transport is generally negative and peaks at −0.5 m³/s/m during fall. Similarly, 2006–2007 also exhibit negative total transport that peak in winter. As for mid-2003 to 2005, total transport in RA2 is about 0.2±0.3 m³/s/m. This analysis reiterates the importance of the wind product used to force an ocean model (e.g., Song et al. 2011), as the difference in wind stress magnitude off Arica and the shift in

Fig. 4 Seasonal wind stress field (in Newton per square meter) based on NCEP R2 over the HCS region averaged from 2000 to 2007. Austral summer (JFM; *top left*), fall (AMJ; *top right*), winter (JAS; *bottom left*), and spring (OND; *bottom right*)

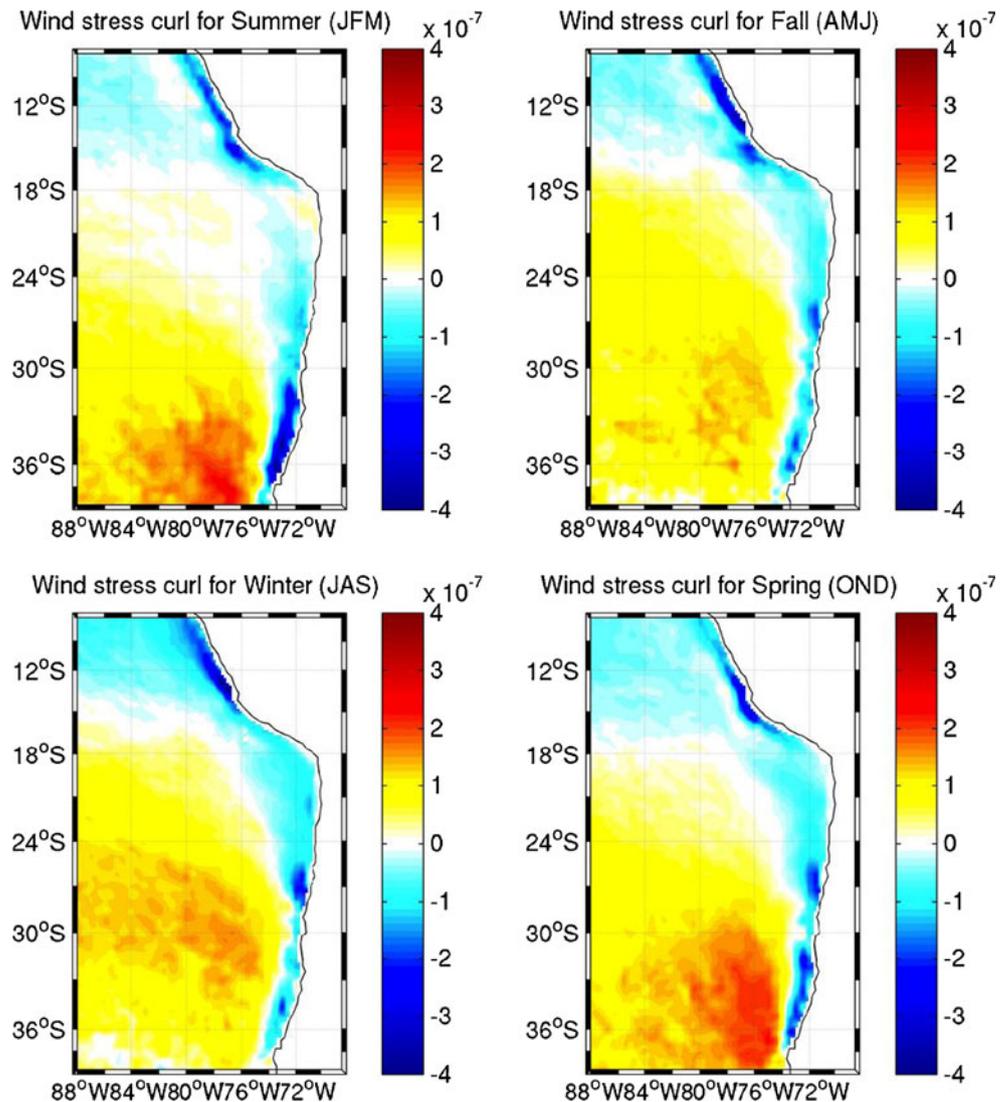the wind stress maximum leads to opposite physical driving mechanisms for nutrient flux.

Comparison of SCOAR winds to RA2 winds along coastal regions shows the differences of their influence on wind-driven upwelling variability and thus the importance of wind products used to test the sensitivity of coastal ocean models (e.g., Capet et al. 2004; Song et al. 2011; Moore et al. 2009). The total upwelling transport in SCOAR and RA2 has seasonally opposite signs at Taltal and Arica, which reflects the importance of the spatial distribution of wind forcing used. In particular, near the coast where differences in wind stress magnitude and location of wind stress maxima, which in turn affects wind stress curl fields, can greatly influence the wind-driven upwelling processes and thus affect at least one factor of nutrient flux. At San Juan, where the seasonal cycle in total upwelling transport is similar, spatial pattern of wind forcing still play an important role

in distinguishing the wind-driven upwelling processes that support the ecosystem.

3.3 Atmospheric boundary layer coupling to mesoscale SST anomalies: wind stresses

Ocean–atmosphere coupling in the HCS is next identified through satellite observations and the simulations of control SCOAR and smoothed SCOAR. Satellite-derived SST products are obtained from the fusion of Tropical Rainfall Measuring Mission Microwave Imager (TMI) data, which is available from November 1997 (Wentz et al. 2000) and from the Advanced Microwave Scanning Radiometer on the Earth Observing System Aqua satellite (AMSR-E) data that available from May 2002 (Wentz and Meissner 2000; Chelton and Wentz 2005). Both TMI and AMSRE data have been combined and optimally space–time interpolated to

Fig. 5 Seasonal wind stress curl field (in Newton per square meter per meter) derived from satellite observations over the HCS region averaged from 2000 to 2007. Austral summer (JFM; *top left*), fall (AMJ; *top right*), winter (JAS; *bottom left*), and spring (OND; *bottom right*)
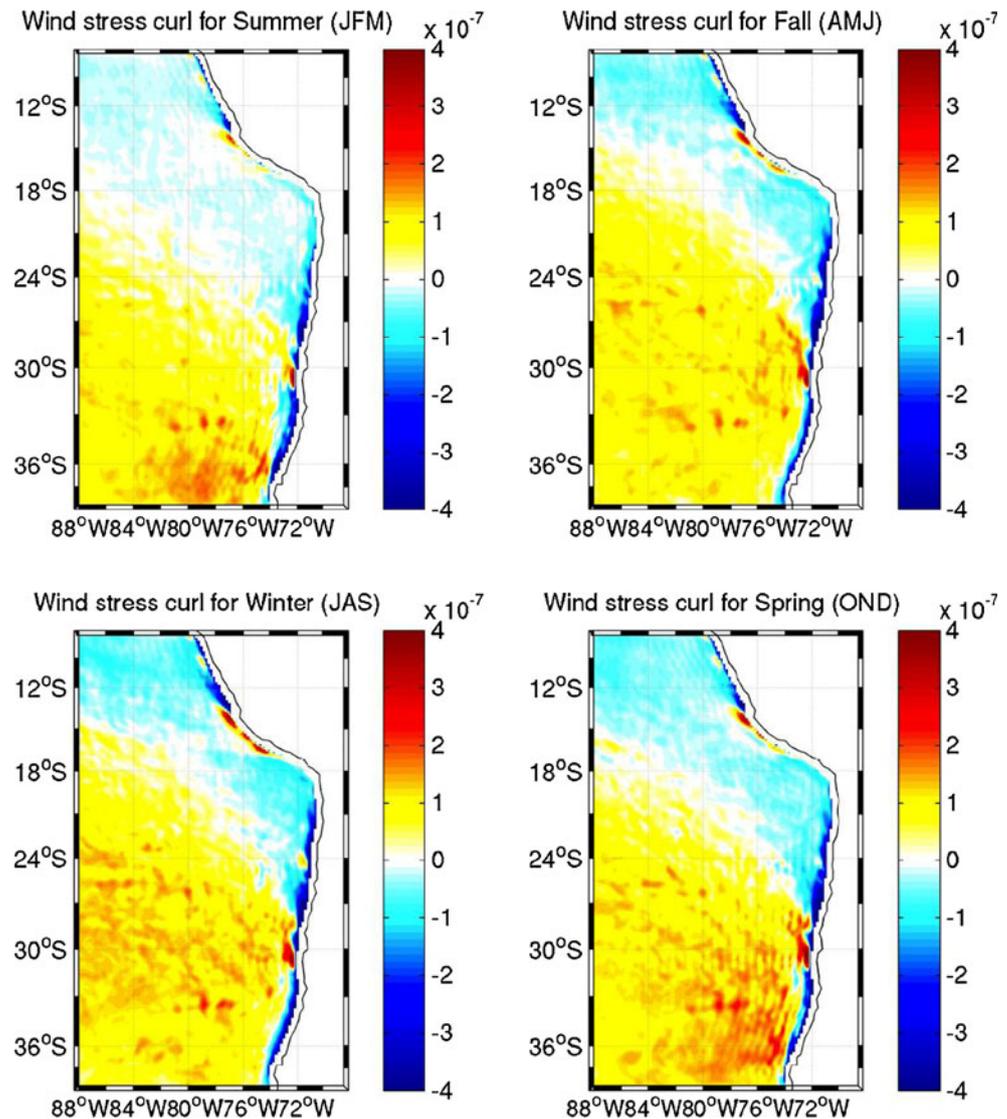

give daily SST products at 0.25° resolution (Reynolds et al. 2004). These data are available on the remote sensing systems.

Using TMI-AMSRE SST data and QSCAT wind stress fields for 2003–2007, monthly downwind SST gradient and crosswind SST gradient, along with corresponding wind stress divergence and convergence are computed. These calculations are also performed with the outputs from control SCOAR and smoothed SCOAR. Figure 11 (left) shows an example of wind stress divergence (in colors) overlaid with contours of downwind SST gradients averaged over April 2007, for control SCOAR, smoothed SCOAR, and satellite observations, respectively. Both control SCOAR as well as satellite observations provide a prominent example of downwind SST gradient underlying wind stress divergence and vice versa on the oceanic mesoscale. In smoothed SCOAR, some overlay exists, but it is not as distinct as control SCOAR, suggesting that smoothing SST fields would reduce the coupling.

For a better quantification of the air–sea coupling, bin scatter plots (Fig. 12, top) of the wind stress divergence against downwind SST gradient are created, and a linear regression is performed on the mean of each bin (Xie 2004; Chelton et al. 2004). The error bars show 1 standard deviation of the wind stress divergence for each bin. The slope of the linear fit (hereinafter designated as the "coupling coefficient", s_d), with its associated standard error and r^2 coefficient, is all evaluated for each case. For April 2007, the coupling coefficients are found to be $s_d=0.9\pm0.2$ for control SCOAR, $s_d=0.1\pm0.3$ for smoothed SCOAR, and $s_d=1.2\pm0.1$ for satellite observations. Control SCOAR produces a comparable coupling coefficient to satellite observations, while smoothed SCOAR does not have the coupling, which indicates the importance of the mesoscale to the air–sea coupling.

These calculations were then extended for each month in 2003–2007. The monthly coupling coefficients (s_d) for control SCOAR (red) and satellite observations (black,

Fig. 6 Seasonal wind stress curl field (in Newton per square meter per meter) over the HCS region averaged from 2000 to 2007 for SCOAR. Austral summer (JFM; *top left*), fall (AMJ; *top right*), winter (JAS; *bottom left*), and spring (OND; *bottom right*)
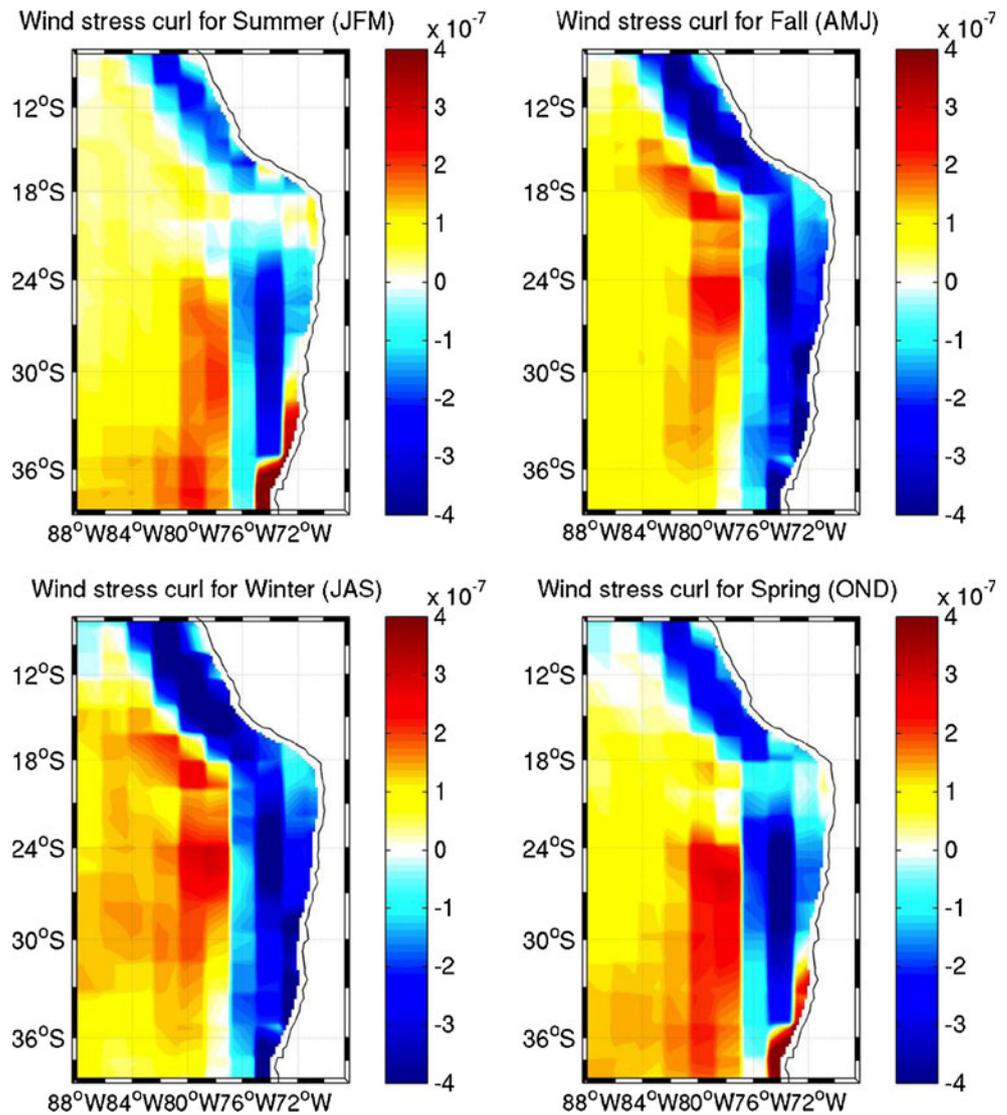

excluding data within 50 km of the coast) along with their confidence intervals measured by the standard error are plotted in Fig. 13 (top). Here, we consider s_d to be significant if its associated r^2 coefficient is greater than 0.6 and its associated p value (based on Students t test) is less than 0.05. If these criteria are not met, s_d is considered insignificant (and marked by a green dot), and their standard errors are not shown. Since smoothed SCOAR produces s_d that are all flagged by this criterion, they have been omitted from Fig. 13 (top). The results reveal a seasonal pattern to the air–sea coupling coefficients in control SCOAR (red) and satellite observations (black). Satellite observations indicate stronger coupling in austral summer and fall, while control SCOAR shows stronger coupling in austral fall and winter. While s_d are comparable in most austral fall months, the model does not capture the precise seasonal cycle found in observations. For smoothed SCOAR, coupling is insignificant, indicating the important role of the oceanic mesoscale

on the coupling of downwind SST gradient and wind stress divergence. Observation-based s_d evaluated in HCS is weaker than its counterpart in the CCS by roughly a factor of 0.5 in summer months (Chelton et al. 2007; Seo et al. 2007a; Haack et al. 2005, 2008; Jin et al. 2009), suggesting that air–sea coupling is not strong in the HCS region.

In a similar fashion, we next analyze the coupling between crosswind SST gradients and wind stress curl (Chelton et al. 2001, 2004). Figure 11 (right) shows the colormap of the wind stress curl (Newton per square meter per 10,000 km) overlaid with contours of crosswind SST gradients averaged over April 2007, for control SCOAR, smoothed SCOAR, and satellite observations, respectively. Likewise, it can be seen that both control SCOAR and satellite observations have indications for air–sea coupling. Performing the linear fit to the bin scatter plot (Fig. 12, bottom), coupling coefficients (s_c) for crosswind SST gradients to wind stress curl are found to be $s_c=0.7\pm0.1$ with r^2

Fig. 7 Seasonal wind stress curl field (in Newton per square meter per meter) based on NCEP R2 over the HCS region averaged from 2000 to 2007. Austral summer (JFM; *top left*), fall (AMJ; *top right*), winter (JAS; *bottom left*), and spring (OND; *bottom right*)

correlation of 0.8 for control SCOAR, $s_c=0.5\pm0.1$ ($r^2=0.5$) for smoothed SCOAR, and $s_c=0.7\pm0.1$ ($r^2=0.8$) for satellite observations. Like the previous analysis, smoothed SCOAR indicates the importance of oceanic mesoscale on air–sea coupling.

The calculations were then extended through 2003–2007, which reveals a seasonal cycle of the air–sea coupling in control SCOAR and satellite observations (Fig. 13, bottom). Observation-derived air–sea coupling shows peaks in austral summer seasons and usually extending to April. However, air–sea coupling based on control SCOAR has significant coupling in austral winter seasons. While positive s_c values between control SCOAR and observations are comparable, the model is unable to capture the details of the seasonal cycle in this case. Air–sea coupling (s_c) in smoothed SCOAR is found to be mostly insignificant (flagged with $r^2<0.6$) and thus not plotted in Fig. 13 (bottom), again suggesting that ocean mesoscale plays an

important role in the coupling of crosswind SST gradient with wind stress curl. For summer months, s_c from observations are approximately a factor of 0.6 lower than those found in CCS (Chelton et al. 2007), which indicates that the intensity of air–sea coupling in the HCS region is relatively weak.

In summary, the control SCOAR produces seasonal coupling coefficients comparable in magnitude to those observed in satellite observations. However, smoothed SCOAR (large-scale coupling) does not produce any significant SST–wind stress coupling throughout the whole run. This may be due to large-scale SST gradients driven by intrinsic oceanic processes being too weak or to large-scale SST gradients being predominantly driven by atmospheric variability. This shows the critical role of mesoscale ocean instabilities in producing the ocean–atmosphere coupling seen in control SCOAR (full-coupled mode) in this region.
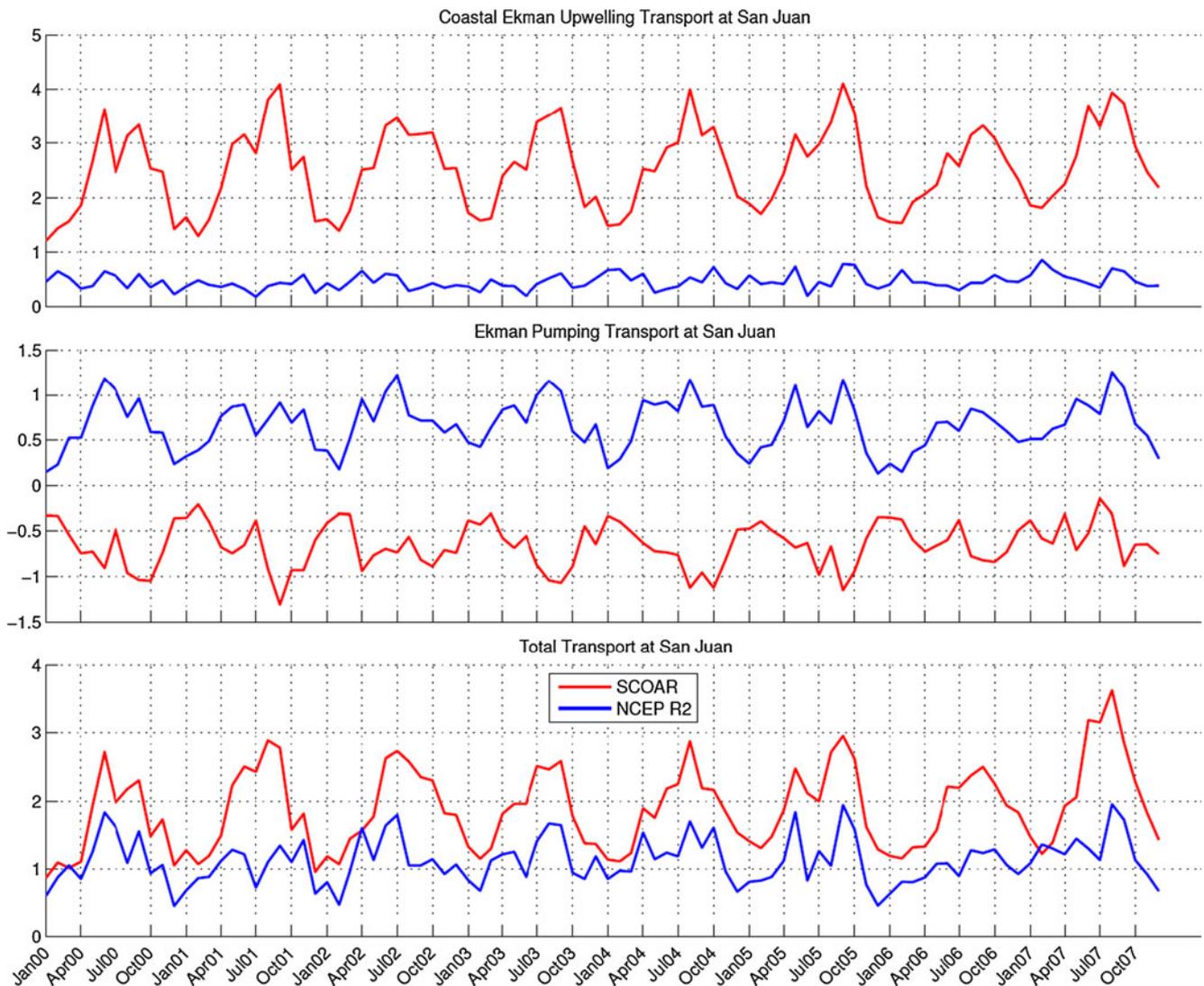
Fig. 8 Time series of coastal Ekman upwelling transport (*top*), Ekman pumping transport (*middle*), and total wind-driven upwelling transport (*bottom*) at San Juan based on SCOAR (*red*) and NCEP R2 (*blue*) over the time period of 2000–2007. Transport is in units of cubic meters per second per meter of coast

3.4 Atmospheric boundary layer coupling to mesoscale SST anomalies: heat fluxes

We next explore the impact of mesoscale SST anomalies on the atmospheric boundary layer by isolating the influence of SST on latent flux anomalies. Latent heat flux out of the ocean can be diagnosed according to the bulk parameterization of Fairall et al. (1996) as LH=rho×L×c_H×U_a×(q_s−q_a) where rho is air density, L is the latent heat of vaporization of water, c_H is the bulk exchange coefficient, U_a is the wind speed at 10 m, q_a is the specific humidity of air near the surface, and q_s is the saturation specific humidity based on SST. It should be noted that latent heat flux in SCOAR is computed using the non-local BL parameterization scheme in RSM, while the relation between the variability of latent heat flux and mesoscale SST patterns is analyzed through the bulk parameterization given above with various parameters that often covary with SST.

A positive linear relation between SST and latent heat flux indicates the influence of SST on latent heat flux in a direct and/or indirect manner. A direct impact of an increase in SST would raise q_s and thus the latent heat flux out of the ocean. This is under the assumption that all other parameters have insignificant changes. Another possibility is the increase in SST would lead to greater instability of the overlying atmosphere that supports turbulent downward mixing of momentum from winds aloft to the surface that would enhance U_a and thus also increase latent heat flux. This would result not only in a positive linear relation between SST and latent heat flux but also a positive linear relation of wind speed with SST, as well as wind speed with latent heat flux.
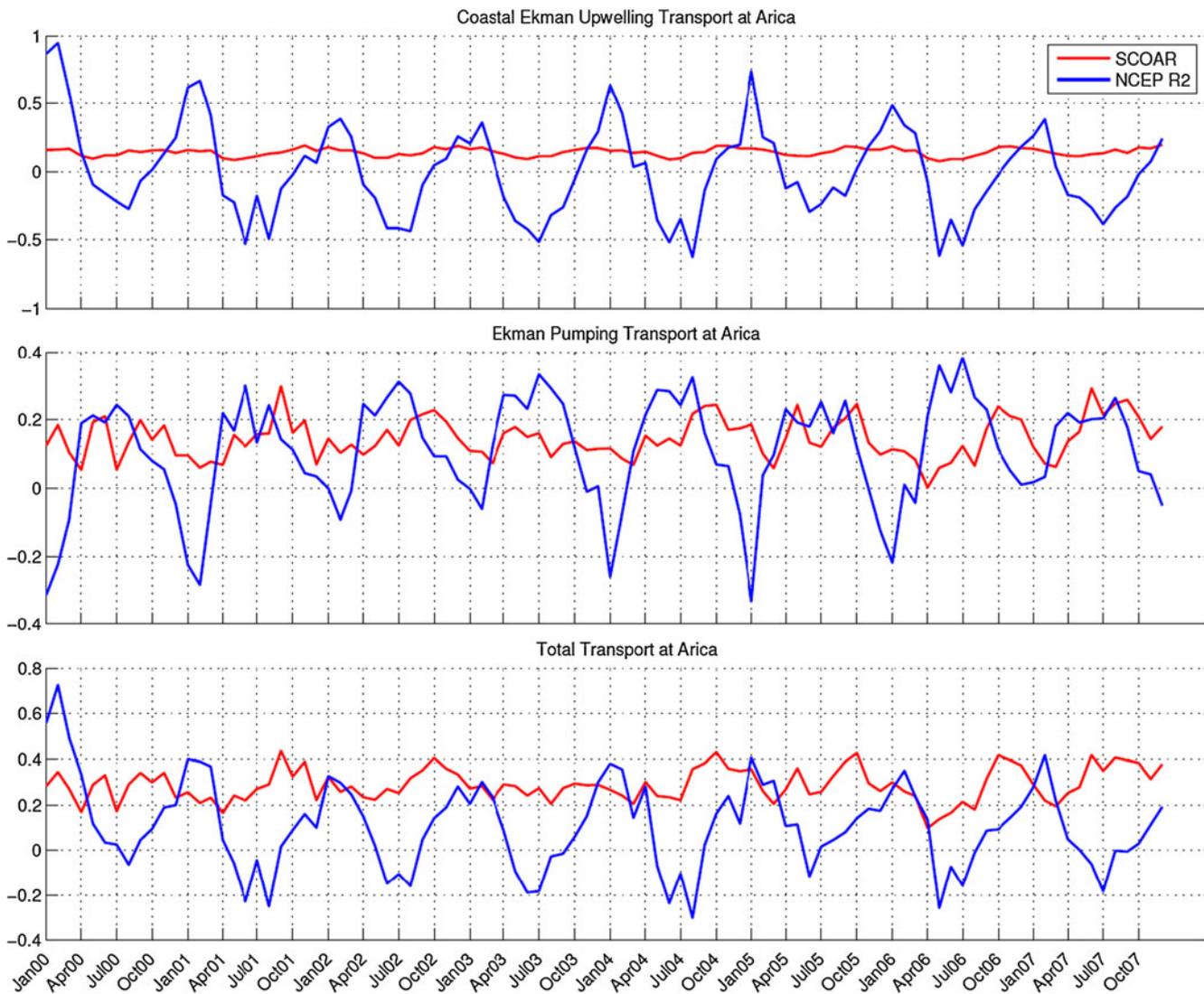
Fig. 9 Same as Fig. 8 but for the coastal water off Arica

Figure 14 shows the distribution of SST, wind speed, and latent heat flux averaged over April 2007 from control SCOAR. It exemplifies the complicated nature of the relationship between latent heat flux, wind speed, and SST. The SST distribution is diagonally divided into two regions, with warmer SSTs to the north and cooler SSTs to the south that decrease as one gets closer to shore. Cooler SSTs are found just off the coast of San Juan (15 S) and along Punta Lavapie (37 S), running north to Coquimbo (30 S). At the bight right off Arica (18 S), a SST maximum is seen. The winds are generally in the northwest direction (based on Figs. 2 and 3) and decrease with higher latitudes. Higher winds in the open ocean north of 24 S generally coincide with warmer SSTs. South of 24 S, winds weaken as one goes offshore and southwards, while SST increases as one goes offshore. Coastal jets with increased winds are seen along San Juan (15 S) and Coquimbo (30 S) in Fig. 14

(middle, red shaded) that collocate with cooler SSTs (Fig. 14, left, bluer shaded), which suggest wind-driven upwelling at these locations. Much reduced winds are found around Arica (18 S) which coincide with the SST maximum. Luff winds around 32 S are located under the anti-cyclonic, subtropical high. The distribution of latent heat flux can be divided into three regions: coastal region off Peru, intensified latent heat flux that runs diagonally in a northwest direction and the southern region (south of intensified region). Low amounts of latent heat flux into the atmosphere are seen right along the coast of Peru that roughly collocates with low SST, but not with wind speed. Over the warm SST region off Arica (17 S–22 S; 76 W to the coast), where wind speed is low, latent heat flux varies considerably from 0 to 90 W/m^2. In the intensified latent heat flux region, high latent heat flux generally coincides with high SST and wind speed. For the southern region, latent heat flux generally
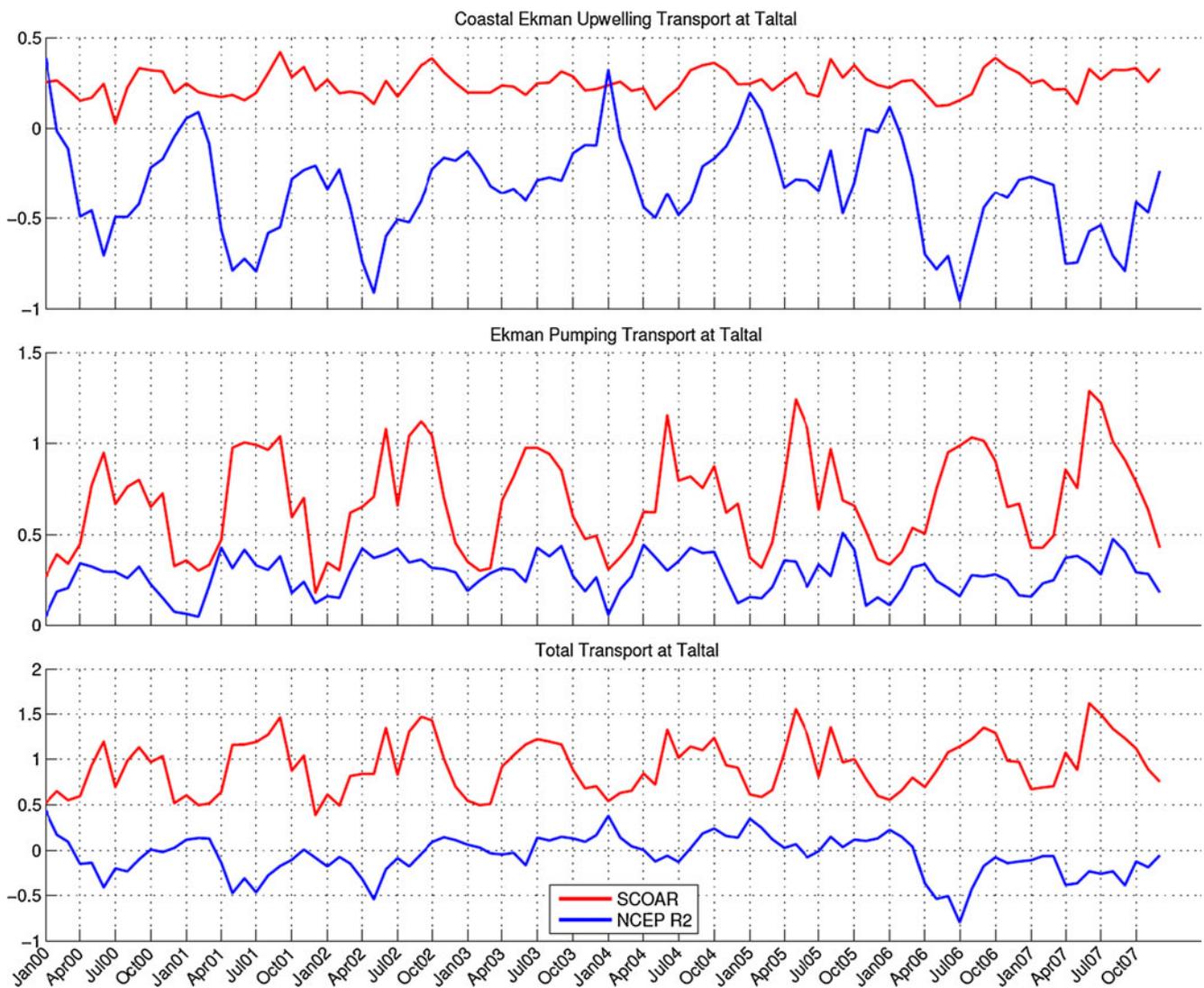
Springer

Fig. 10 Same as Fig. 8 but for the coastal water off Taltal

decreases with latitude, like wind speed. However, a zonal gradient in latent heat flux is not seen, unlike in SST and wind speed.

More quantified measures of the relationships between latent heat flux, SST, and wind speed are shown in Fig. 15 as scatterplots of latent heat flux against SST, wind speed against SST, and latent heat flux against wind speed for April 2007 for the whole HCS domain. A linear regression is performed on each scatterplot to obtain coupling coefficients (s_{full}) and its associated r^2 correlation coefficient. For latent heat flux against SST, a positive linear relation of s_{full} =5.2 W/m^2/°C is found, with only a small fraction of the variance explained (r^2=0.31). Similarly, a positive linear relationship is found for wind speed and SST (s_{full}= 0.6 m/s/°C), with an associated r^2=0.28. As for latent heat flux and wind speed, s_{full}=4.1 W/m^2 per m/s with r^2 of 0.24. Even though a positive linear relationship is found for all

three cases, the spread of the data points is very large, and the fraction of variance explained (r^2 correlation coefficient) for each case is small. This suggests that in the full-coupling scenario (control SCOAR), SST does contribute but it is not the main driver to latent heat flux, whether directly through increased flux or indirectly through turbulent mixing.

Likewise, the same linear regression analysis is performed for smoothed SCOAR (not shown), and the results for s_{large} are very similar to control SCOAR. The data points from smoothed SCOAR are smeared within the confines of the spread in data points from control SCOAR, which leads to similar coupling coefficients and associated r^2 values for both control SCOAR and smoothed SCOAR. For latent heat flux and SST, we find that s_{large}=5.0 W/m^2/°C with r^2=0.31. As for wind speed and SST, s_{large}=0.6 m/s/°C with r^2=0.29. And for latent heat flux against wind speed, s_{large}=4.0 W/m^2 per m/s with r^2=0.25. Again, the fraction of variance explained
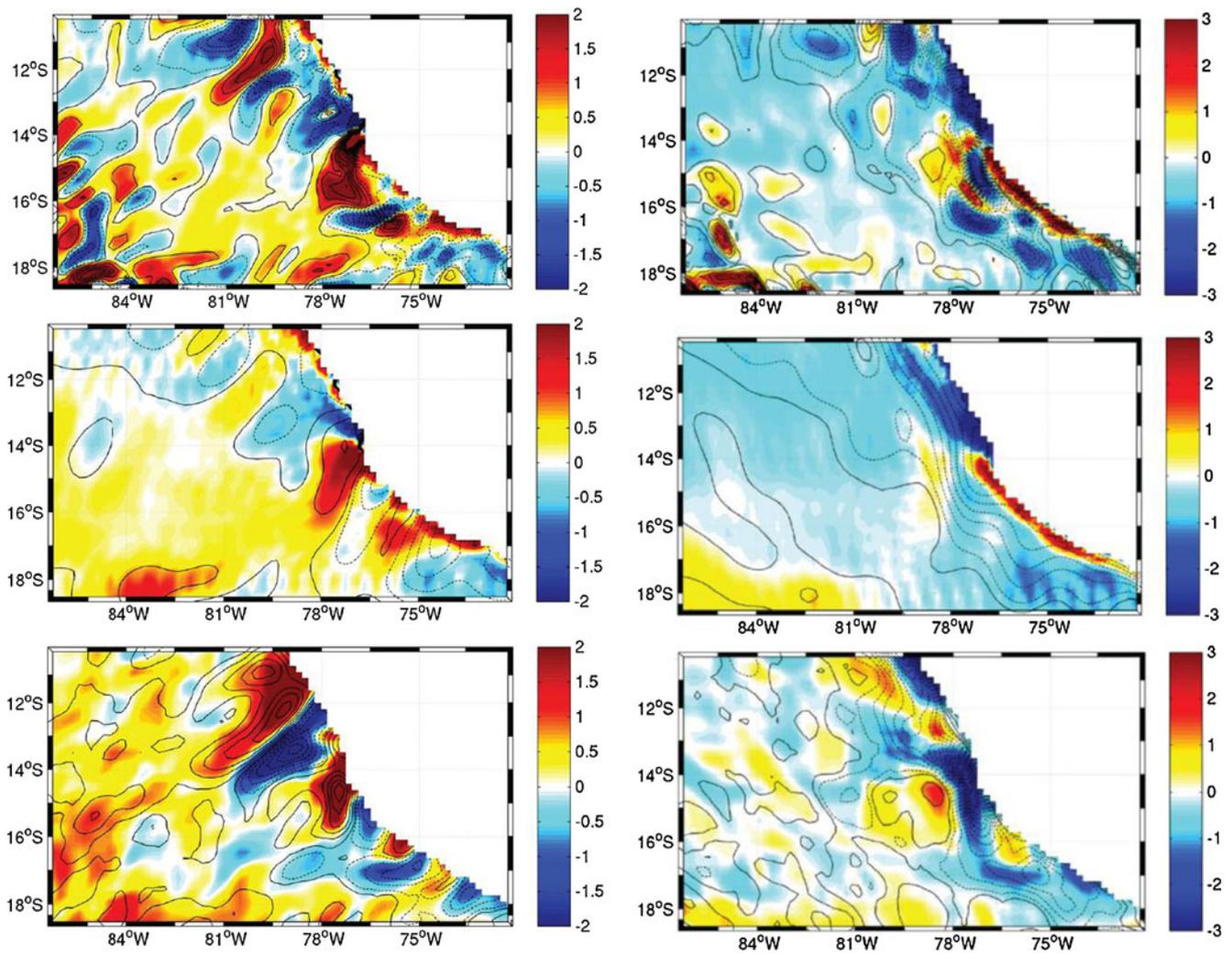
Fig. 11 *Left* Colormap of wind stress divergence (in Newton per square meter per 10,000 km) averaged for April 2007, overlaid with contours of downwind SST gradients (in degree Celsius per 100 km) over the Peru domain for *top* control SCOAR, *middle* smoothed SCOAR, and *bottom* satellite observations. *Solid* (*dashed*) contours

indicate positive (negative) downwind SST gradients at 0.4 °C per 100 km intervals. *Right* Same, but for wind stress curl (in Newton per square meter per 10,000 km) overlaid with contours of crosswind SST gradients (in degree Celsius per 100 km)

for each case is small, indicating that SST can contribute but is not the main driver of latent heat flux when only large-scale coupling is considered (smoothed SCOAR).

While the direct and indirect impact of SST on latent heat flux is not dominant under full coupling and large-scale coupling, this does not preclude the significance of mesoscale SST impact on latent heat flux. A direct-differencing comparison of SST impact cannot be done with control and smoothed SCOAR runs because the oceanic eddies are randomly generated in each case. So in order to extract the mesoscale SST impact, a comparative differencing study is executed between control SCOAR and smoothed RSM (using smoothed SST fields from control SCOAR to force the atmosphere). Figure 1 shows how the filter affects the control SCOAR SST field for April 2007. The difference of the SST fields between the two cases ranges between ±0.5 °C. At latitudes above 18 S, most

of the differences occur along the coastal background SST front, which stretches to roughly 2° offshore, where anomalous advection by mesoscale eddies drives large SST differences. A diagonal corridor of strong SST differences stretches along the background SST front from the shoreline around (74 W, 23 S) to roughly (88 W, 16 S) with negligible SST differences to the north and south of the mean front. South of 21 S, larger SST differences concentrate along the background SST front that extends from the shoreline to approximately 6° offshore, with reduced SST differences beyond that.

Figure 16 (top) shows the latent heat flux for April 2007 for the two cases. At first glance, it seems that the latent heat flux has been directly smoothed out from control SCOAR (left panel) onto smoothed RSM (middle panel). However, the middle panel is a reflection of the latent heat flux into the atmosphere from implementing smoothed SST fields. The
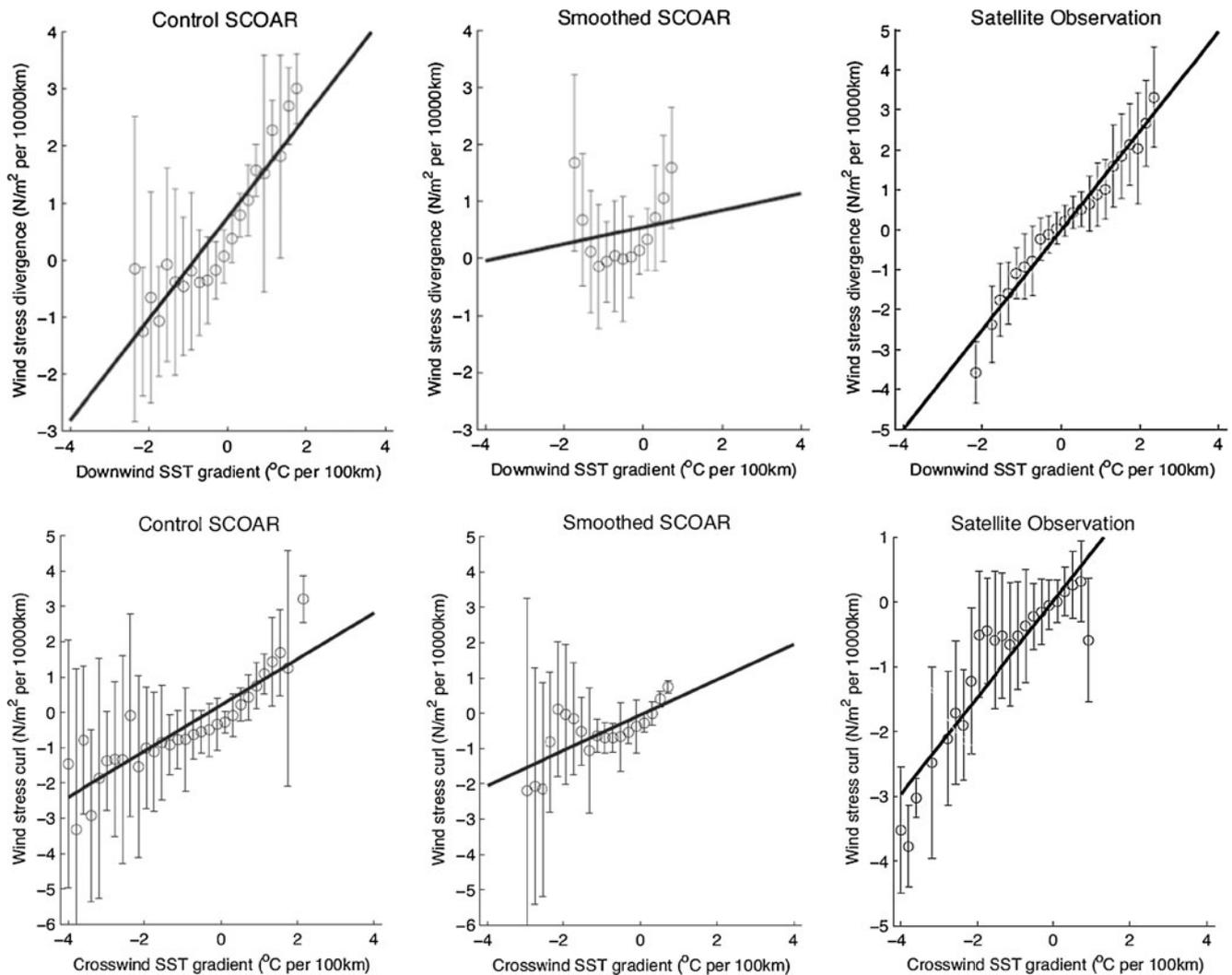
Fig. 12 *Top* Bin scatter plots of wind stress divergence (in Newton per square meter per 10,000 km) against downwind SST gradients (in degree Celsius per 100 km), averaged for April 2007 over the Peru domain for control SCOAR, smoothed SCOAR, and satellite observations. *Error bars* are 1 standard deviation of each bin. *Bottom* Same as top, but for wind stress curl (in Newton per square meter per 10,000 km) against crosswind SST gradients (in degree Celsius per 100 km)

right panel gives the percentage of change in latent heat flux into the atmosphere from the two cases. It highlights similar features to the structure and magnitude of SST changes seen in Fig. 1, but with a large range in the percentage latent heat change of ±30 %. North of 18 S, the difference in latent heat flux is also confined along the shoreline and extends 2–4° offshore. Intensified percentage change in latent heat flux is seen to the south of the diagonal corridor.

Since latent heat flux is also affected by surface wind speed, similar plots are made for wind speed (Fig. 16, bottom) for comparison. Again, the middle panel gives the wind speed distribution when forced by smoothed SST fields from control SCOAR, and the right panel is the percentage of change in wind speed between control SCOAR and smoothed RSM. With the exception of a diagonal corridor of negligible (less than 1 %) wind speed

percentage change, the rest of the domain shows mesoscale wind speed changes that range between ±5 %.

Rather than the percentage change, Fig. 17 (top) shows the actual difference between control SCOAR and smoothed RSM for latent heat flux, SST, and wind speed. Both wind speed and latent heat flux mesoscale patterns that are strikingly similar to the mesoscale SST anomalies. As such, scatter plots of these three *mesoscale* quantities in relation to one another are constructed in Fig. 17 (bottom) to provide a better quantification on the impact of the mesoscale SST features. Similar to the coupling coefficients defined previously, the coupling coefficients (s_{meso}) here are defined by the slope to the linear fit of the scatterplots. Note that s_{meso} extracts out the impact of only the mesoscale SST upon the latent heat flux, while previously, s_{full} includes coupling on the large scale and mesoscale, and s_{large} is only for coupling at the large scale.
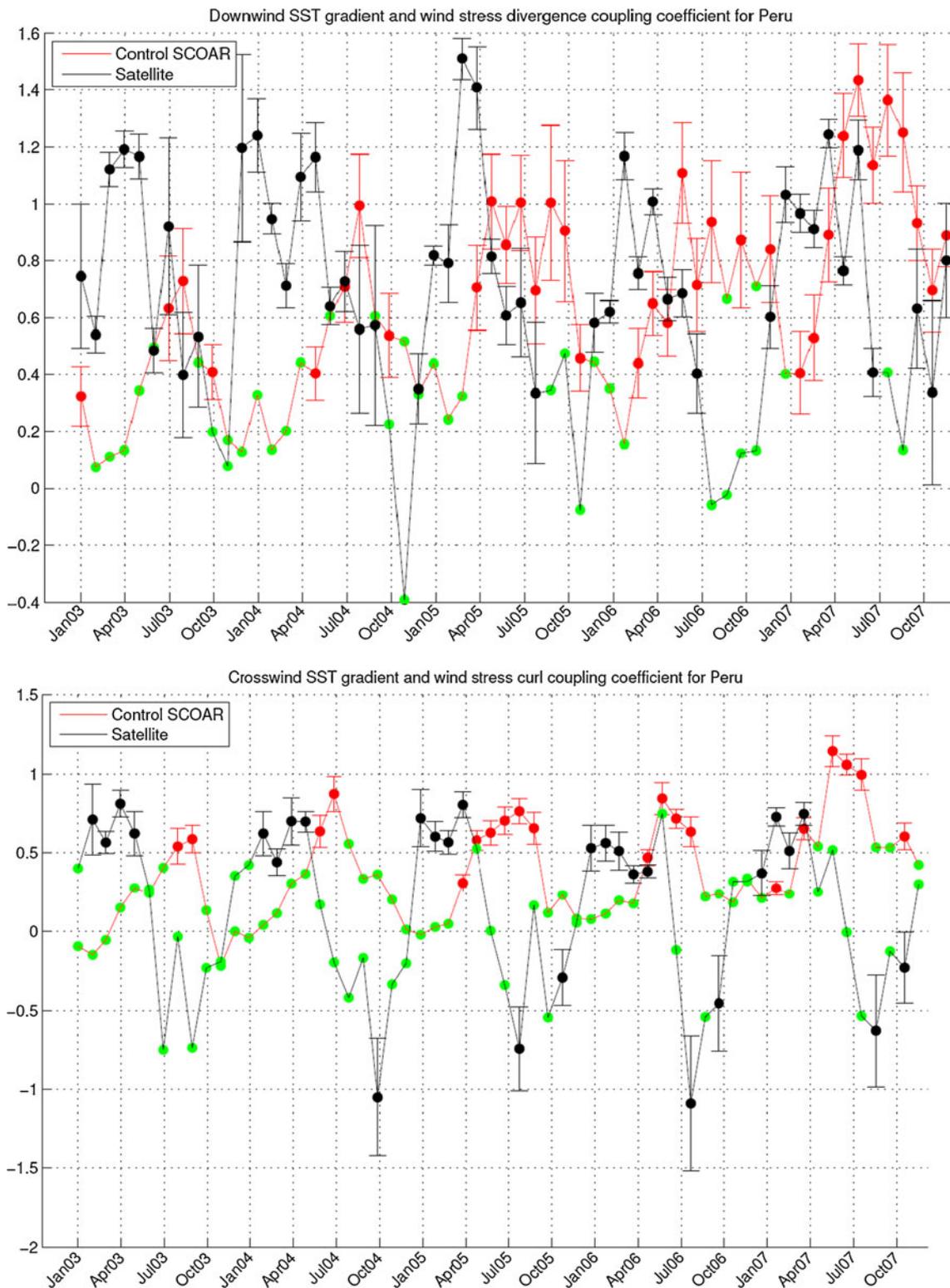
Fig. 13 *Top* Time series of monthly coupling coefficients (s_d) over the Peru domain for control SCOAR (*red*) and satellite observations (*black*). *Green dots* indicate that the slopes have r^2 correlation less than 0.6 and/or *p* values greater than 0.05. *Error bars* are standard errors of the slopes. *Bottom* Same as top, but for coupling coefficients (s_c)

The coupling between the difference in latent heat flux to the difference in SST is $s_{meso}=19$ W/m^2/°C (with $r^2=0.86$), which is a significant coupling. It suggests that SST is the main driver of latent heat flux at the mesoscale. The "split"
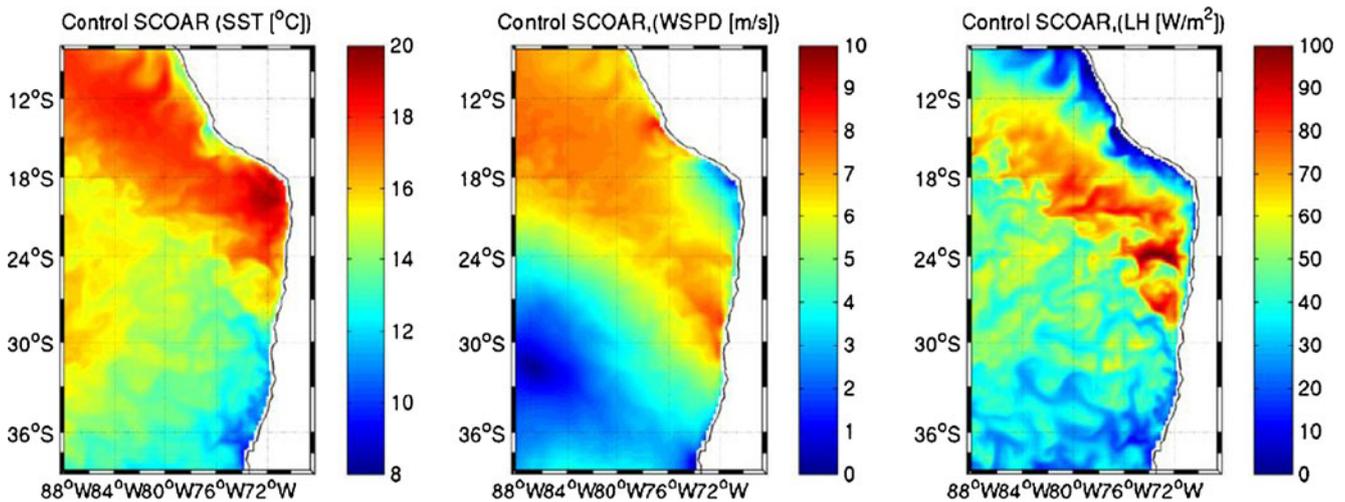
Fig. 14 Averaged SST distribution (in degree Celsius; *left*), wind speed distribution (in meters per second; *middle*), and latent heat flux into the atmosphere distribution (in Watts per square meter; *right*), over April 2007 from control SCOAR

in the scatterpoints at the tail ends of the SST differences (bottom left of Fig. 17) suggests that mesoscale SST is driving latent heat flux in two different regions associated with two different slopes. The stronger slope corresponds to the regions of higher background wind speed (Fig. 16, bottom), which increases coupling strength in the bulk formula. This generates the greatest impacts along the large background SST frontal regions that run diagonally across the domain and along the offshore coastal areas of Peru.

A significant linear fit of the difference in wind speed and difference in SST is also observed with s_{meso}=0.27 m/s/°C at r^2=0.70. This indicates the influence of warmer (colder) mesoscale SST on enhancing (reducing) surface winds that is most likely due to the increased (decreased) vertical turbulent mixing that transports momentum from winds

aloft to the surface. There is also significant coupling between the difference in latent heat flux and the difference in wind speed, with s_{meso}=57 W/m² per m/s at r^2=0.85. This reinforces the idea that mesoscale SST can have a direct influence on latent heat flux, as well as through increased (decreased) atmospheric instability that leads to greater (smaller) surface winds and thus enhances (reduces) latent heat flux.

The calculation for mesoscale coupling coefficients, s_{meso}, was extended to include each month from 2000–2007 and is shown in Fig. 18. There is no clear seasonal cycle in s_{meso}, although a trend is seen from 2006 onward, which has no obvious explanation. In general, mesoscale coupling between wind speed and SST is significant, which promotes the influence of SST on atmospheric stability and
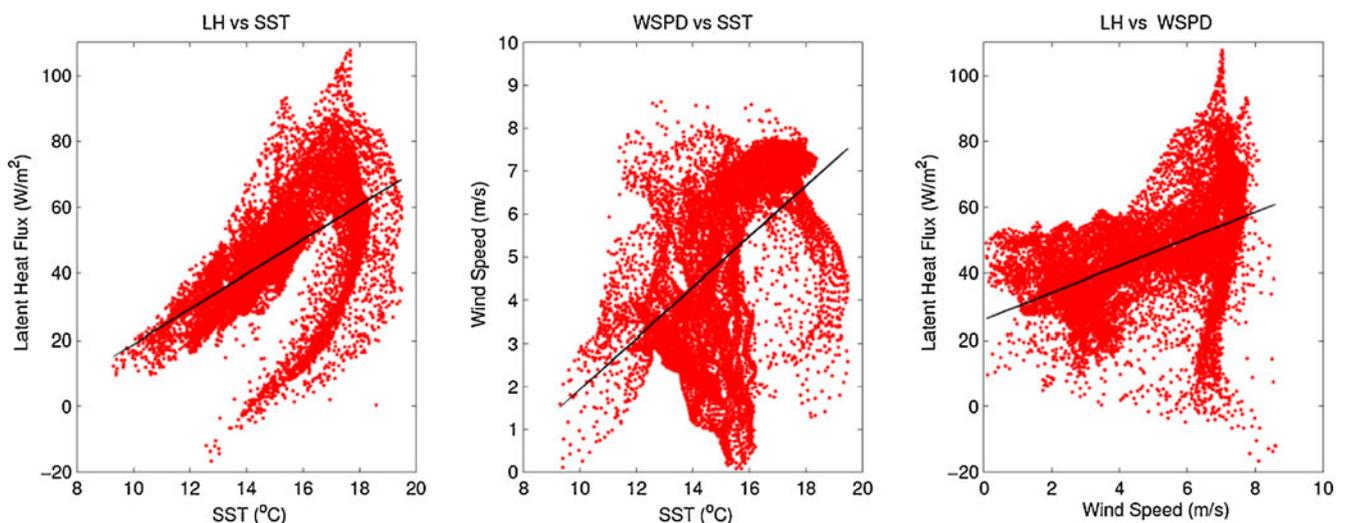

Fig. 15 Scatter plots of latent heat flux against SST (*left*), wind speed against SST (*middle*), and latent heat flux against wind speed (*right*). All based on averaged April 2007 values from control SCOAR. The slope of the linear fits give the coupling coefficients, s_{full}
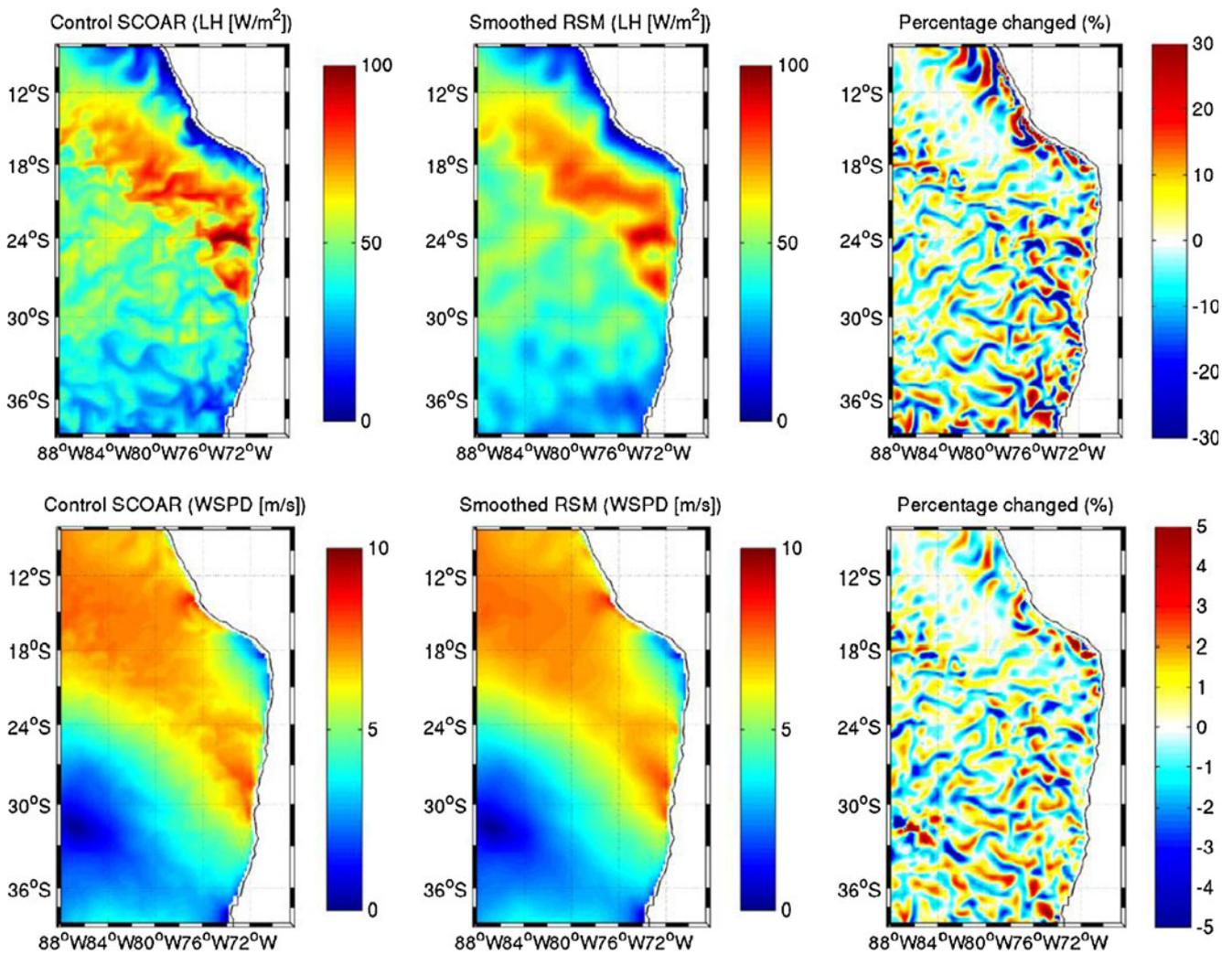
Fig. 16 *Top* April 2007 averaged latent heat flux (out of the ocean) distribution over entire model domain for control SCOAR (*left*), smoothed RSM (*center*), and the percentage of their difference (*right*). *Bottom* Same as *top*, but for wind speed (meters per second). Compare these plots with the corresponding SST plots in Fig. 1

surface winds at the mesoscale. Mesoscale coupling between latent heat flux and SST is significant throughout. When both types of mesoscale coupling are significant, it likely that both direct and indirect influences of SST to latent heat flux are at work. At times when mesoscale coupling of wind speed and SST are insignificant (flagged by $r^2 < 0.5$), the indirect influence of mesoscale SST through atmospheric stability and surface winds would not be significant, suggesting that the direct influence of mesoscale SST on latent heat flux is the main process by which mesoscale SST drives latent heat.

Using the strategy of smoothing SST fields from control SCOAR and applying it to an uncoupled atmosphere (smoothed RSM), the impact of mesoscale coupling is extracted. Coupling between latent heat flux, SST, and wind speeds is not easily identified in the fully coupled mode (control SCOAR) and large-scale-coupled mode (smoothed

SCOAR). However, once the coupling on the mesoscale (smoothed RSM) is isolated, significant coupling is found between latent heat flux, SST, and wind speeds.

A similar analysis was conducted to identify the imprints of mesoscale SST on the overlying atmosphere, e.g., the atmospheric boundary layer thickness, clouds, etc. However, the effects were found to be local and small (~5 % or less) and did not appear to generate a broader-scale, rectified response, either spatially or temporally (not shown) in this part of the World Ocean.

3.5 Ocean eddy response to coupled surface flux anomalies

The downscaled wind stress field in SCOAR drives a vigorous mean and eddy circulation in the ocean component of the coupled model, comparable to that obtained for the HCS with uncoupled versions of ROMS (e.g., Colas et al. 2008,
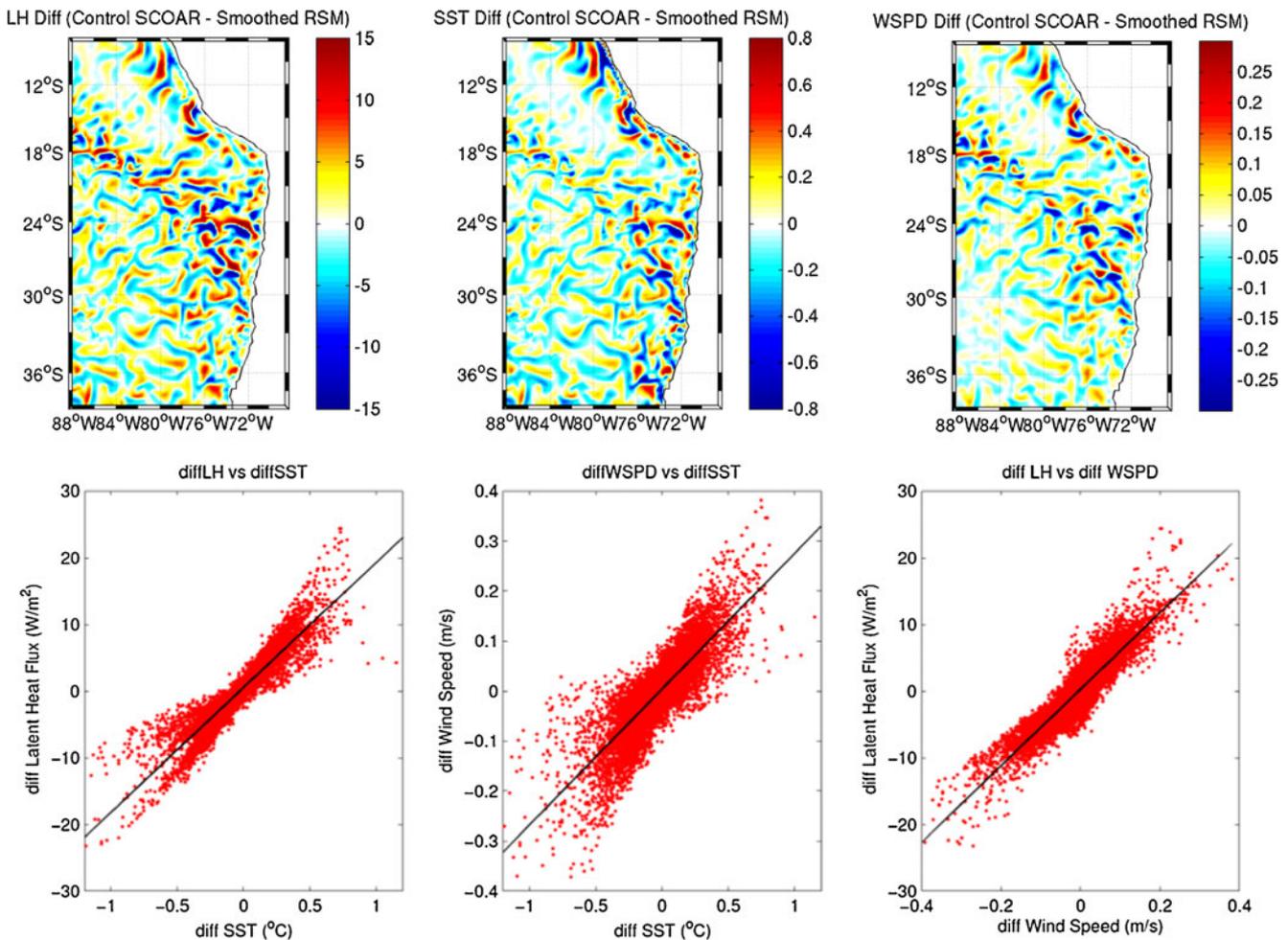
Fig. 17 *Top* Colormaps of difference between control SCOAR and smoothed RSM for latent heat flux (in Watts per square meter; *left*), SST (in degree Celsius; *middle*), and wind speed (in meters per second; *right*), all based on averaged April 2007 values. *Bottom* Scatter plots of difference in latent heat flux against difference in SST (*left*), difference in wind speed against difference in SST (*middle*), and difference in latent heat flux against difference wind speed (*right*) from fields plotted above. The slope of the linear fits gives the coupling coefficients, s_{meso}

2012; Combes et al. 2013; Subramanian et al. 2013). SST–wind stress coupling, however, can exert a potentially important impact on baroclinic instability in the ocean and hence the on the properties of mesoscale eddies. For example, within an idealized framework, Spall (2007) showed that along gradients in SST, with winds blowing from warm to cold waters, the SST–wind stress coupling would act to increase the wavelength and growth rate of the most unstable waves, and vice versa.

Here we consider, in a full-physics dynamical framework, a comparative study of mesoscale eddy statistics using control SCOAR and smoothed SCOAR. This allows an investigation of the impact of full coupling, which has SST–wind stress coupling based on previous section, versus large-scale coupling, which does not have mesoscale SST–wind stress coupling, upon the ocean eddy statistics. Recall that the main difference between the two run is that in smoothed SCOAR, the atmosphere only sees a smoothed

version of the SST field from ROMS, but ROMS is allowed to freely evolve at the same grid resolution as that in control SCOAR. In addition, for comparison, an uncoupled oceanic run, smoothed ROMS, is studied to assess the influence of spatially smoothed surface forcing on the ocean.

Figure 19 shows the root-mean-square (RMS) distribution of SST for control SCOAR (left), smoothed SCOAR (middle), and smoothed ROMS (right). Control SCOAR and smoothed SCOAR have very similar SST variability distribution. Both show larger SST variability in the southwest portion of the domain, as well as along the coast, particularly around San Juan region and Taltal. On the other hand, smoothed ROMS has much reduced SST variability along the coast. In the open ocean, the SST variability of smoothed ROMS reveals a spatial pattern with larger amplitude SST variance somewhat similar to those of control SCOAR and smoothed SCOAR. The altered pattern of SST variability, which is more pronounced along the coast, is
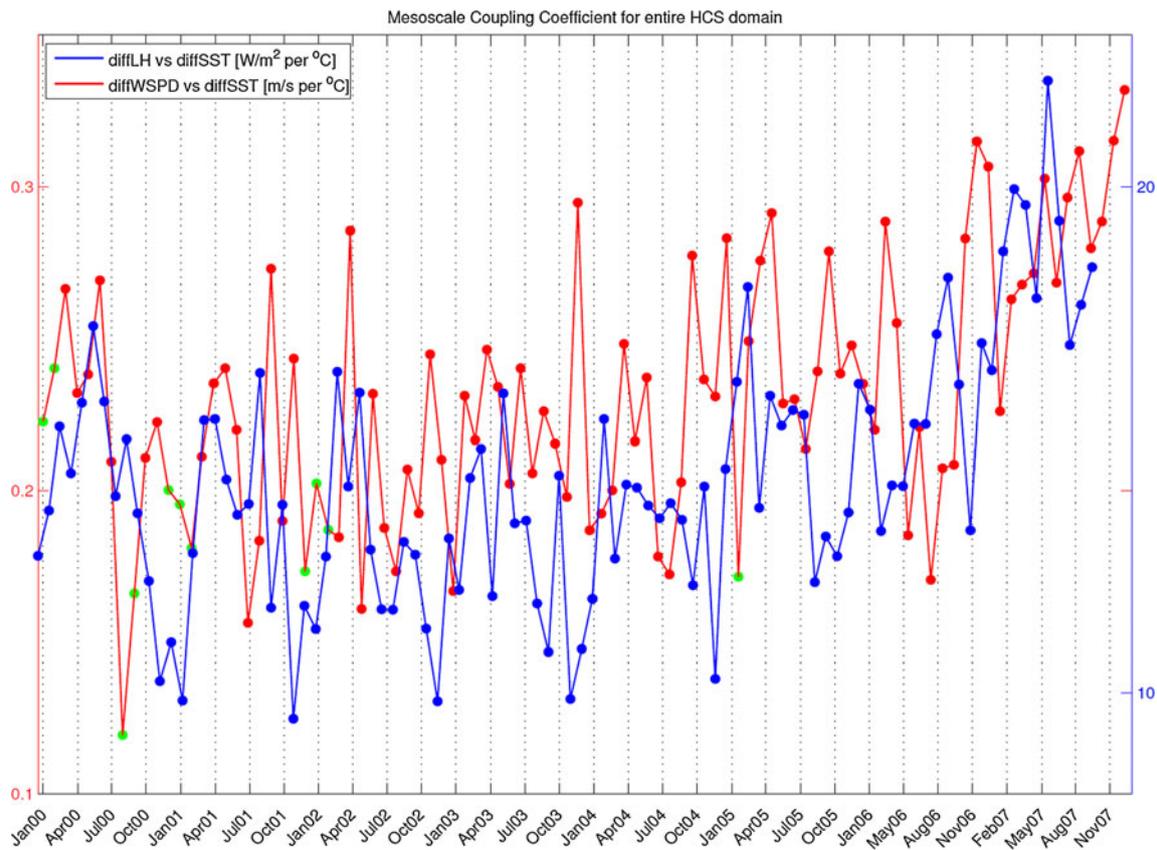
Fig. 18 Time series of monthly mesoscale coupling coefficients (s_{meso}) for difference in latent heat against difference in SST (*blue*; in Watts per square meter per degree Celsius; *right axis*) and difference in wind speed against difference in SST (*red*; meters per second per degree Celsius; *left axis*). *Green dots* indicate that the slopes have r^2 correlation less than 0.5 and/or p values greater than 0.05

clearly due to the smoothing of the forcing fields. Figure 20 shows the seasonal wind stress pattern used in smoothed ROMS, which has reduced the magnitude of the wind stress along the coast and shifted maximum wind stress offshore when compared to Fig. 3 for the fully coupled model. This consequently alters the mean ocean circulation along with the stability properties of the eddies that develop upon it (e.g., Moore et al. 2009; Song et al. 2011), as we examine next.

Further understanding of ocean eddy activity can be quantified using the vorticity of surface currents. Figure 21
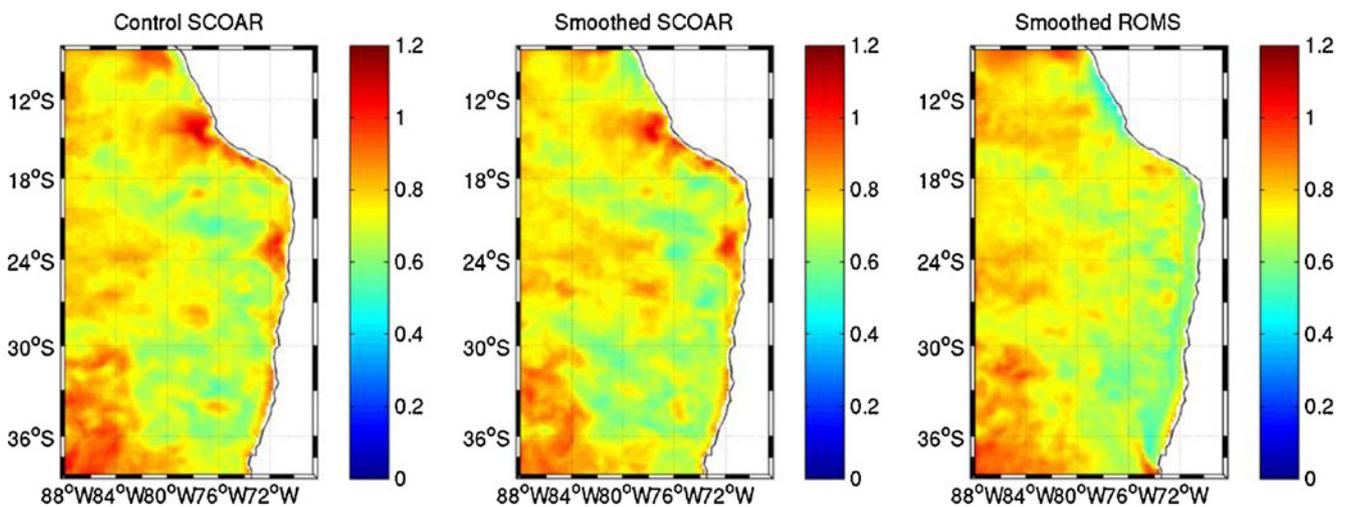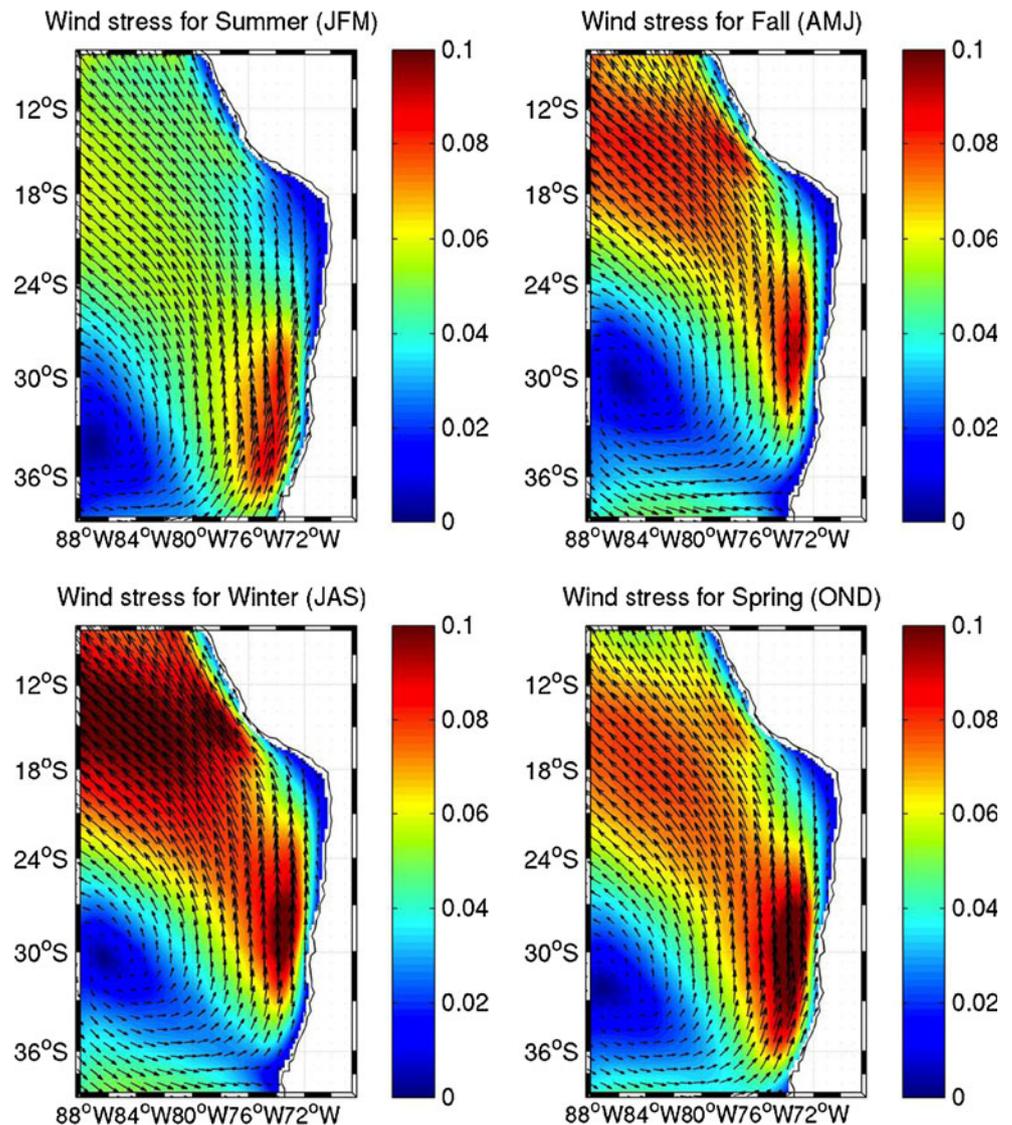

Fig. 19 Spatial distribution of root mean square of SST (in degree Celsius) for control SCOAR (*left*), smoothed SCOAR (*middle*), and smoothed ROMS (*right*) for the time period of 2000–2007

Fig. 20 Seasonal wind stress field (in Newton per square meter) based on smoothed ROMS over the HCS region averaged from 2000 to 2007. Austral summer (JFM; *top left*), fall (AMJ; *top right*), winter (JAS; *bottom left*), and spring (OND; *bottom right*)
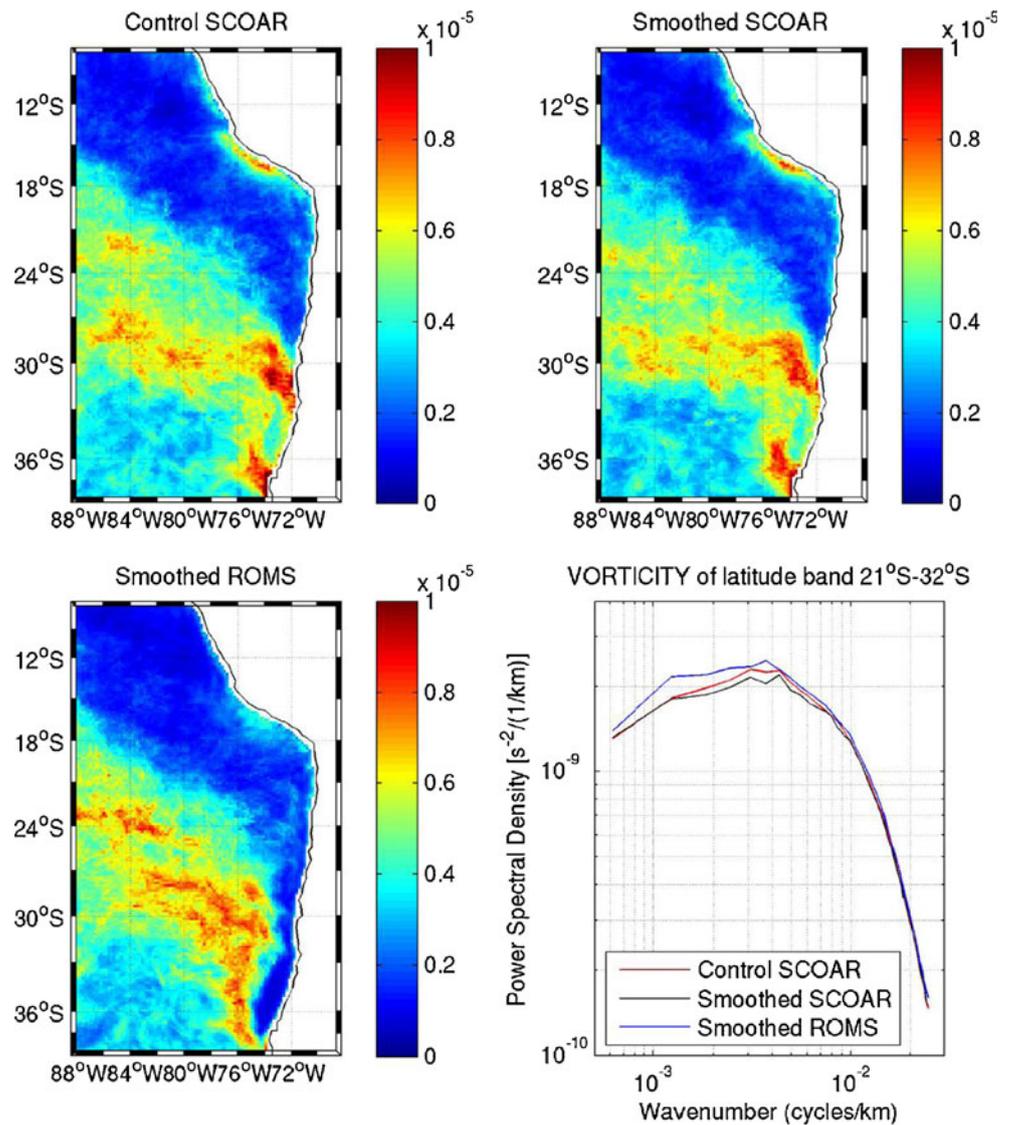

presents RMS vorticity over the model domain for control SCOAR, smoothed SCOAR, and smoothed ROMS. Again, the coupled cases show similar RMS distribution, with greater variability in vorticity seen in upwelling regions such as San Juan, Coquimbo, and Punta Lavapie, where instability sets up and eddies are generated. A diagonal divider from (72 W, 28 S) to (88 W, 16 S) separates a region of minimal vorticity variability to the north and a region of intensified variability in ocean eddies to the south. South of 32 S, the vorticity variability in the open sea dips by a factor of half from the intensified region. As for smoothed ROMS, the general RMS distribution of vorticity is somewhat similar to the coupled case. However, along the coast, this variability has been significantly reduced, which is clearly due to the smoothed forcing fields driving a different mean flow and eddy instability pattern. The power spectrum of the vorticity in latitudinal band 21 S–32 S for control SCOAR and smoothed SCOAR is of the same shape and peak at the

same wavelength (200–300 km), with only a very weak increase in energy of eddies in the mesoscale band for control SCOAR compared to smoothed SCOAR. This suggests that the SST–wind stress coupling does not have a strong impact on the ocean eddies in the HCS. It is likely that the weak SST gradients and the relatively weak SST–wind stress coupling found in HCS contribute to the lack of a strong response of the ocean eddies.

The power spectrum of the vorticity (Fig. 21) shows that the coupled case contains less energy than the uncoupled smoothed ROMS run for wavelengths larger than 250 km (note that the power spectrum is computed using roughly 130,000 data record series [45 records for each day of 2000–2007], so even small differences in spectra are very likely to be significant). This may indicate that large-scale air–sea feedback works to reduce this eddy energy. However, this is not definitive because of the spatial structure of the atmospheric forcing along the coast. In smoothed ROMS, the

Fig. 21 Spatial distribution of root mean square of surface vorticity (in per second) for control SCOAR (*top left*), smoothed SCOAR (*top right*), and smoothed ROMS (*bottom left*) for the time period of 2000–2007. *Bottom right panel* shows the power spectrum of surface vorticity for latitude band 21 S–32 S for control SCOAR (*red*), smoothed SCOAR (*black*), and smoothed ROMS (*blue*)

displacement of the wind stress peak offshore (Fig. 20) changes the mean field of the forcing along the coast and sets up a different mean state for ocean circulation and eddy generation. As such, the instability properties that arise from a different mean state have changed, and the ocean eddies cannot be directly compared to one another. The difference in the power spectrum between the uncoupled smoothed ROMS and the coupled case could thus be attributed to either the different mean state of the ocean generating more energetic instabilities or to the absence of air–sea coupling feedback allowing more energetic ocean eddies.

The feedback on the ocean from full coupling (control SCOAR) and large-scale coupling (smoothed SCOAR) does not produce strong differences in the ocean eddy statistics in the HCS. This suggests that removal of mesoscale features onto the atmosphere does not produce any rectification that would affect the HCS ocean eddies. It is possible that the SST gradients in the HCS, as well as the SST–wind stress

coupling, may not be strong enough to produce results similar to what Spall (2007), Pezzi et al. (2004), or Hogg et al. (2009) found. We also explored changes in wavelengths and in sea-surface height in the eddy regions of the model domain, but these analyses also only produced very small changes. We are currently exploring the changes in eddy statistics due to mesoscale coupling in the Kuroshio Current region, where strong SST gradients produce much larger coupling coefficients (Putrasahan et al. 2013) and more energetic ocean eddies.

4 Summary and discussion

Regional coupled ocean–atmosphere processes were studied in a SCOAR downscaling of the 2000–2007 time period in the HCS. First, the downscaled control SCOAR seasonal wind stress patterns were shown to be superior to those of

the base fields (RA2) when compared against satellite observations. Then, various aspect of oceanic, atmospheric, and ocean–atmosphere responses were investigated using the fully coupled model and tandem coupled (smoothed SCOAR), and uncoupled (smoothed RSM, smoothed ROMS) runs designed to isolate the impact of the oceanic mesoscale SST anomalies.

The more highly resolved wind stress product was assessed in its potential impact as a forcing function for coastal Ekman upwelling and in open-ocean Ekman pumping. The sign and magnitude of Ekman pumping and Ekman offshore transport was found to be strongly regionally sensitive to the choice of wind stress forcing products, which indicates that caution should be used when invoking wind products for assessing nutrient flux estimates for sustaining ecosystems. At Taltal and Arica, the total wind-driven upwelling transport in SCOAR and RA2 has seasonally opposite signs because of the difference in the spatial distribution of the wind-forcing product. In an upwelling zone such as San Juan, wind-driven upwelling in SCOAR is dominated by coastal Ekman upwelling, while in RA2 upwelling is mostly attributed to Ekman pumping.

The impact of mesoscale SST anomalies on wind stress anomalies was assessed using differences of ocean–atmosphere coupling in control versus smoothed SCOAR. This component of mesoscale coupling was found to be significant and comparable in amplitude to observations in control SCOAR, but the annual cycle found in observations was not reproduced in the model. Smoothed SCOAR showed no significance in SST–wind stress coupling throughout most of the run, which indicates the importance of the role of ocean mesoscale eddies on SST–wind stress coupling.

An assessment of the coupling between SST, wind speed, and latent heat flux within the context of a fully coupled mode found no coherent coupling for control SCOAR or smoothed SCOAR. However, the difference fields for (control SCOAR–smoothed RSM) yield significant coupling between latent heat flux, SST, and wind speed. The positive correlation between SST and surface wind speed at the mesoscale suggests that mesoscale SST anomalies have an imprint on the overlying atmospheric stability, which affects the vertical mixing of momentum onto surface mesoscale wind. Since significant coupling is also seen between mesoscale wind speed and latent heat flux as well as SST and latent heat flux at the mesoscale, the imprint of mesoscale SST on latent heat flux is attributed to both a direct influence of SST on the heat flux, as well as indirectly through the stability changes in the atmosphere that affects wind speeds and thus the latent heat flux, all at the mesoscale.

The effect of SST–surface–flux coupling on ocean eddies was explored by comparing the statistics of SST anomalies and surface current vorticity in control SCOAR, smoothed SCOAR, and smoothed ROMS. Maps of RMS fields and

plots of the power spectra do not reveal any strong differences in the runs. This suggests that the SST–surface–flux coupling does not exert a strong impact on the ocean eddies in the HCS. This is likely due to the weaker SST gradients and seasonally dependent SST–wind stress coupling found in this region. Additional research needs to be done to determine if these effects act more efficiently in more energetic ocean regions, such as a the Kuroshio Extension region where Putrasahan et al. (2013) found stronger coupling effects.

References

Bryan F, Tomas R, Dennis J, Chelton D, Loeb N, McClean J (2010) Frontal scale air–sea interaction in high-resolution coupled climate models. J Climate 23:6277–6291

Capet XJ, Marchesiello P, McWilliams JC (2004) Upwelling response to coastal wind profiles. Geophys Res Lett 31:L13311. doi:10.1029/2004GL020123

Castelao RM, Barth JA (2006) Upwelling around Cabo Frio, Brazil: the importance of wind stress curl. Geophys Res Lett 33:L03602. doi:10.1029/2005GL025182

Cayan DR (1992) Latent and sensible heat flux anomalies over the northern oceans: driving the sea surface temperature. J Phys Oceanogr 22:859–880

Chelton D, Esbensen S, Schlax M, Thum N, Freilich M, Wentz F, Gentemann CL, McPhaden M, Schopf P (2001) Observations of coupling between surface wind stress and sea surface temperature in the eastern tropical Pacific. J Climate 14:1479–1498

Chelton D, Schlax M, Freilich M (2004) Satellite measurements reveal persistent small-scale features in ocean winds. Science 303:978–983

Chelton D, Schlax M, Samelson R (2007) Summertime coupling between sea surface temperature and wind stress in the California Current System. J Phys Oceanogr 37:495–517

Chelton D, Wentz F (2005) Global microwave satellite observations of sea surface temperature for numerical weather prediction and climate research. Bull Am Meteorol Soc 86:1097–1115

Chelton D, Xie SP (2010) Coupled ocean–atmosphere interaction at oceanic mesoscales. Oceanogr 23:52–69

Colas F, Capet X, McWilliams JC, Shchepetkin A (2008) 1997–98 El Nino off Peru: a numerical study. Progr Ocean 79:138–155

Colas F, McWilliams JC, Capet X, Kurian J (2012) Heat balance and eddies in the Peru–Chile current system. Clim Dynam 39:509–529

Combes V, Di Lorenzo E, Gomez F, Hormazabal S, Strub TP, Putrasahan D (2013) Low-frequency variability of upwelling and cross-shelf transport in the Humboldt Current System. J Phys Oceanogr (submitted)

Fairall C, Bradley E, Rogers D, Edson J, Young G (1996) Bulk parameterization of air–sea fluxes for tropical ocean global

atmosphere coupled ocean–atmosphere response experiment. J Geophys Res 101:3747–3764

Garreaud RD, Munoz RC (2005) The low-level jet off the west coast of subtropical South America: structure and variability. Mon Wea Rev 133:2246–2226

Haack T, Burk SD, Hodur RM (2005) U.S. West Coast surface heat fluxes, wind stress, and wind stress curl from a mesoscale model. Mon Wea Rev 133:3202–3216

Haack T, Chelton D, Pullen J, Doyle J, Schlax M (2008) Summertime influence of SST on surface wind stress off the U.S. west coast from the U.S. Navy COAMPS model. J Phys Oceanogr 38:2414–2437

Haidvogel DB, Arango H, Budgell WP, Cornuelle BD, Curchitser E, Di Lorenzo E, Fennel K, Geyer WP, Hermann AJ, Lanerolle L, Levin J, McWilliams JC, Miller AJ, Moore AM, Powell TM, Shchepetkin AF, Sherwood CR CR, Signell RP, Warner JC, Wilkin J (2008) Ocean forecasting in terrain-following coordinates: formulation and skill assessment of the Regional Ocean Modeling System. J Comput Phys 227:3595–3624

Halpern D (2002) Offshore Ekman transport and Ekman pumping off Peru during the 1997–1998 El Nino. J Geophys Res 29:191–194

Hogg AM, Dewar WK, Berloff P, Kravtsov S, Hutchinson DK (2009) The effects of mesoscale ocean–atmosphere coupling on the large-scale ocean circulation. J Climate 22:4066–4082

Hong SY, Pan HL (1996) Nonlocal boundary layer vertical diffusion in a medium-range forecast model. Mon Wea Rev 124:2322–2339

Jin X, Dong C, Kurian J, McWilliams JC, Chelton DB, Li Z (2009) SST–wind interaction in coastal upwelling: oceanic simulation with empirical coupling. J Phys Oceanogr 39:2957–2970

Juang HMH, Hong SY, Kanamitsu M (1997) The NCEP regional spectral model: an update. Bull Am Meteorol Soc 78:2125–2143

Juang HMH, Kanamitsu M (1994) The NMC nested regional spectral model. Mon Wea Rev 122:3–26

Kanamitsu M, Ebisuzaki W, Woolen J, Potter J, Fiorino M (2002a) NCEP-DOE AMIP-II Reanalysis (R-2). Bull Am Meteorol Soc 83:1631–1643

Kanamitsu M, Kumar A, Juang HMH, Schemm JK, Wang W, Yang F, Hong SY, Peng P, Chen W, Moorthi S, Ji M (2002b) NCEP dynamical seasonal forecast system 2000. Bull Am Meteorol Soc 83:1019–1037

Large WG, Danabasoglu G (2006) Attribution and impacts of upper-ocean biases in CCSM3. J Climate 19:2325–2346

Lim KSS, Hong SY (2010) Development of an effective double-moment cloud microphysics scheme with prognostic cloud condensation nuclei (CCN) for weather and climate models. Mon Wea Rev 138:1587–1612

Liu W (2002) Progress in scatterometer application. J Oceanogr 58:121–136

Liu WT, Xie X, Niiler PP (2007) Ocean–atmosphere interaction over Agulhas Extension meanders. J Climate 20:5784–5797

Ma CC, Mechoso C, Robertson A, Arakawa A (1996) Peruvian stratus clouds and the tropical Pacific circulation: a coupled ocean–atmosphere GCM study. J Climate 9:1635–1645

Minobe S, Miyashita M, Kuwano-Yoshida A, Tokinaga H, Xie S-P (2010) Atmospheric response to the Gulf Stream: seasonal variations. J Climate 23:3699–3719

Moore AM, Arango HG, Di Lorenzo E, Miller AJ, Cornuelle BD (2009) An adjoint sensitivity analysis of the Southern California Current circulation and ecosystem. J Phys Oceanogr 39:702–720

Nakamura H, Sampe T, Tanimoto Y, Shimpo A (2004) Observed associations among storm tracks, jet streams and midlatitude oceanic fronts. In: Wang C, Xie S-P, Carton JA (eds) Earth's climate: the ocean–atmosphere Interaction. Geophys Monogr 147, pp 329–346

Nonaka M, Xie S-P (2003) Covariations of sea surface temperature and wind over the Kuroshio and its extension: evidence for ocean-to-atmosphere feedback. J Climate 16:1404–1413

O'Neill L, Chelton D, Esbensen S (2003) Observations of SST-induced perturbations of the wind stress field over the southern ocean on seasonal time scales. J Climate 16:2340–2354

O'Neill L, Chelton D, Esbensen S, Wentz F (2005) High-resolution satellite measurements of the atmospheric boundary later response to SST variations along the Agulhas return current. J Climate 18:2706–2723

Overland JE, Alheit J, Bakun A, Hurrell JW, Mackus DL, Miller AJ (2010) Climate controls on marine ecosystems and fish populations. J Mar Sys 79:305–315

Pezzi LP, Vialard J, Richard KJ, Menkes C, Anderson D (2004) Influence of ocean–atmosphere coupling on the properties of tropical instability waves. Geophys Res Lett 31:L16306. doi:10.1029/2004GL019995

Pickett MH, Paduan JD (2003) Ekman transport and pumping in the California Current based on the U.S. Navy's high-resolution atmospheric model (COAMPS). J Geophys Res 108. doi:10.1029/2003JC001902

Putrasahan DA, Miller AJ, and Seo H. (2013) Isolating mesoscale coupled ocean–atmosphere interactions in the Kuroshio Extension region. Dyn Atmos Oceans (in press)

Putrasahan DA (2012) Mesoscale coupled ocean–atmosphere feedbacks in boundary current systems. Ph.D. dissertation, University of California, San Diego

Renault L, Dewitte B, Falvey M, Garreaud R, Echevin V, Bonjean F (2009) Impact of atmospheric coastal jet off central Chile on sea surface temperature from satellite observations (2000–2007). J Geophys Res 114. doi:10.1029/2008JC005083

Reynolds RW, Gentemann CL, Wentz F (2004) Impact of TRMM SSTs on a climate-scale SST analysis. J Climate 17:2938–2952

Samelson R, Skyllingstad E, Chelton D, Esbensen S, O'Neill L, Thum N (2006) On the coupling of wind stress and sea surface temperature. J Climate 19:1557–1566

Sasaki H, Sasai Y, Nonaka M, Masumoto Y, Kawahara S (2006) An eddy-resolving simulation of the quasi-global ocean driven by satellite-observed wind field: preliminary outcomes from physical and biological fields. J Earth Simul 6:34–49

Schlax M, Chelton D, Freilich M (2001) Sampling errors in wind fields constructed from single and tandem scatterometer datasets. J Atmos Ocean Tech 18:1014–1036

Seo H, Jochum M, Murtugudde R, Miller A (2006) Effect of ocean mesoscale variability on the mean state of tropical Atlantic climate. Geophys Res Lett 33(L09606). doi:10.1029/2005GL025651

Seo H, Miller A, Roads J (2007a) The Scripps Coupled Ocean–atmosphere Regional (SCOAR) model, with applications in the eastern Pacific sector. J Climate 20:381–402

Seo H, Jochum M, Murtugudde R, Miller AJ, Roads JO (2007b) Feedback of tropical instability wave-induced atmospheric variability onto the ocean. J Climate 20:5842–5855

Seo H, Murtugudde R, Jochum M, Miller AJ (2008) Modeling of mesoscale coupled ocean–atmosphere interaction and its feedback to ocean in the western Arabian Sea. Ocean Model 25:120–131

Shchepetkin A, McWilliams J (2005) The Regional Oceanic Modeling System (ROMS): a split-explicit, free-surface, topography-following-coordinate ocean model. Ocean Model 9:347–404

Sherman K, Hempel G (2008) The UNEP large marine ecosystem report: a perspective on changing conditions in LME's of the world's regional seas. Tech Rep 182 United Nations Environment Programme. Nairobi, Kenya

Small R, de Szoeke S, O'Neill L, Seo H, Song Q, Cornillon P, Spall M, Minobe S (2008) Air–sea interaction over ocean fronts and eddies. Dyn Atmos Oceans 45:274–319

Smith RL (1968) Upwelling. Oceanogr Mar Biol Ann Rev 6:11–46

Song H, Miller AJ, Cornuelle BD, Di Lorenzo E (2011) Changes in upwelling and its water sources in the California Current System driven by different wind forcing. Dyn Atmos Oceans 52:170–191

Spall M (2007) Effect of sea surface temperature–wind stress coupling on baroclinic instability in the ocean. J Phys Oceanogr 37:1092–1097

Subramanian AC, Miller AJ, Cornuelle B, Di Lorenzo E, Weller RA, Straneo F (2013) A data assimilative perspective of oceanic mesoscale eddy evolution during VOCALS-REx. Atmos Chem Phys 13:3329–3344

Thum N, Esbensen S, Chelton D, McPhaden M (2002) Air–sea heat exchange along the northern sea surface temperature front in the eastern tropical Pacific. J Climate 15:3361–3378

Vecchi G, Xie S, Fischer A (2004) Ocean–atmosphere covariability in the western Arabian sea. J Climate 17:1213–1224

Wallace J, Mitchell T, Deser C (1989) The influence of sea surface temperature on surface wind in the eastern equatorial Pacific: seasonal and interannual variability. J Climate 2:1492–1499

Wallace J, Smith C, Jiang Q (1990) Spatial patterns of atmosphere–ocean interaction in the northern winter. J Climate 3:990–998

Wentz F, Gentemann C, Smith D, Chelton D (2000) Satellite measurements of sea surface temperature through clouds. Science 288:847–850

Wentz F, Meissner T (2000) Algorithm theoretical basis document (ATBD) Version 2: AMSR ocean algorithm. Technical Report 121599A Remote Sensing Systems

Wood R. and 23 co-authors (2011) The VAMOS Ocean–Cloud–Atmosphere–Land Study Regional Experiment (VOCALS-REx): goals, platforms, and field operations. Atmos Chem Phys 11:627–654. doi:10.5194/acp-11-627-2011

Xie S-P (2004) Satellite observations of cool ocean–atmosphere interaction. Bull Am Meteorol Soc 85:195–209